Anisotropic cold plasma modes in chiral vector Maxwell-Carroll-Field-Jackiw electrodynamics

Filipe S. Ribeiro,[1,*] Pedro D. S. Silva,[1,†] and Manoel M. Ferreira, Jr.[2,‡]

[1]*Programa de Pós-graduação em Física, Universidade Federal do Maranhão, Campus Universitário do Bacanga, São Luís (MA), 65080-805, Brazil*

[2]*Departamento de Física, Universidade Federal do Maranhão, Campus Universitário do Bacanga, São Luís (MA), 65080-805, Brazil*

(Received 20 December 2023; accepted 21 February 2024; published 2 April 2024)

In this work, we study the propagation and absorption of plasma waves in the context of the Maxwell-Carroll-Field-Jackiw (MCFJ) electrodynamics with a purely spacelike background playing the role of the anomalous Hall conductivity, concerning the anomalous Hall current. Such a current is also found in an axion field which increases linearly with a space coordinate. The Maxwell equations are rewritten for a cold, uniform, and collisionless fluid plasma model, allowing us to determine the new refractive indices and propagating modes. The analysis begins for propagation along the magnetic axis, examined in the cases of chiral vectors parallel and orthogonal to the magnetic field. Two distinct refractive indices (associated with right-handed circularly polarized [RCP] and left-handed circularly polarized [LCP] waves) are obtained and the associated propagation and absorption zones are determined. The low-frequency regime is discussed and we obtain RCP and LCP helicons. We scrutinize optical effects, such as birefringence and dichroism, and observe rotatory power sign reversion, a property of chiral MCFJ plasmas. We also examine the case of transversal propagation in the direction orthogonal to the magnetic field, providing much more involved results.

DOI: 10.1103/PhysRevD.109.076003

I. INTRODUCTION

The propagation properties of electromagnetic waves in a cold magnetized plasma is based on the standard Maxwell equations to describe radio-wave propagation in the ionosphere [1–6]. The interaction of electromagnetic waves and atmosphere has attracted the attention of researchers over the years, including new investigations on reflection, absorption, and transmission in topical plasma scenarios [7]. The cold plasma limit is adopted to study the fluid plasma behavior under the action of a constant external magnetic field [8–13], being defined when the excitation energies are small, so that the thermal and collisional effects can be neglected. In this regime, the ions can be taken as infinitely massive, in such a way that they do not respond to electromagnetic oscillations, especially high-frequency waves. The cold plasma behavior is then described by considering first-order differential equations written for the electron number density n and the electron fluid velocity $\mathbf{u}$, namely,

$$\frac{\partial n}{\partial t}+\boldsymbol{\nabla}\cdot(n\mathbf{u})=0, \tag{1}$$

$$\frac{\partial \mathbf{u}}{\partial t}+\mathbf{u}\cdot\nabla\mathbf{u}=\frac{q}{m}(\mathbf{E}+\mathbf{u}\times\mathbf{B}_0), \tag{2}$$

where $\mathbf{B}_0$ represents the average magnetic field, and q and m stand for the (electron) charge and mass. The linearized version of the magnetized cold plasmas considers fluctuations around average quantities, n_0 and $\mathbf{B}_0$, which are constant in space and time. Following the usual procedure, assuming $\mathbf{B}_0=B_0\hat{z}$, the corresponding plasma dielectric tensor is

$$\varepsilon_{ij}(\omega)=\varepsilon_0\begin{bmatrix} S & -iD & 0\\ iD & S & 0\\ 0 & 0 & P\end{bmatrix}, \tag{3}$$

where ε_0 is the vacuum electric permittivity, and

$$S=1-\frac{\omega_p^2}{(\omega^2-\omega_c^2)},\quad D=\frac{\omega_c\omega_p^2}{\omega(\omega^2-\omega_c^2)},\quad P=1-\frac{\omega_p^2}{\omega^2}, \tag{4}$$

with $\omega_p=n_0q^2/(m\epsilon_0)$ and $\omega_c=|q|B_0/m$ being the plasma and cyclotron frequencies, respectively.

*filipe.ribeiro@discente.ufma.br, filipe99ribeiro@hotmail.com
†pedro.dss@ufma.br, pdiego.10@hotmail.com
‡manojr.ufma@gmail.com, manoel.messias@ufma.br

From the Maxwell theory, two distinct refractive indices are obtained for longitudinal propagation to the magnetic field, $\mathbf{k}\|\mathbf{B}_0$,

$$n_\pm = \sqrt{1 - \frac{\omega_p^2}{\omega(\omega \pm \omega_c)}}, \tag{5}$$

which provide right-handed circularly polarized (RCP) and left-handed circularly polarized (LCP) modes [1]. This is the standard result of wave propagation in the usual magnetized cold plasma. The refractive indices (5) present the cutoff frequencies $\omega_\pm$,

$$\omega_\pm = \frac{1}{2}(\sqrt{\omega_c^2 + 4\omega_p^2} \mp \omega_c), \tag{6}$$

defining limits for the propagation and absorption zones. As for propagation orthogonal to the magnetic field, $\mathbf{k}\perp\mathbf{B}_0$, $\mathbf{k} = (k_x, k_y, 0)$, it is found that the corresponding transversal mode, $\delta\mathbf{E} = (0, 0, \delta E_z)$, is associated with the refractive index

$$n_T = \sqrt{1 - \frac{\omega_p^2}{\omega^2}}, \tag{7}$$

while the extraordinary longitudinal mode, $\delta\mathbf{E} = (\delta E_x, \delta E_y, 0)$ is related to [13]

$$n_O = \sqrt{\frac{(S+D)(S-D)}{S}}, \tag{8}$$

with P, S, and D given in Eq. (4). The refractive index n_T provides a linearly polarized propagating mode, whereas n_O, in general, is related to an elliptically polarized mode.

In condensed matter systems, chiral media are endowed with optical activity [14] stemming from parity-odd models, as bi-isotropic [15] and bi-anisotropic electrodynamics [16–21], where circularly polarized waves propagate at distinct phase velocities, yielding birefringence and optical rotation [22]. Such an optical activity is due to anisotropies of the matter structure or can be implied by external fields (Faraday effect [23–25]), being measured in terms of rotatory power (RP) [26]. Magneto-optical effects constitute a useful tool to investigate new materials, such as topological insulators [27–35] and graphene compounds [36].

In the context of modified electrodynamics, the Maxwell-Carroll-Field-Jackiw (MCFJ) electrodynamics was initially proposed to examine the possibility of CPT and Lorentz violation (LV) in free space, establishing severe constraints on the magnitude of the LV coefficients [37]. This model also represents the CPT-odd piece of the $U(1)$ gauge sector of the broad Standard Model extension (SME) [38]. The SME has been extensively examined by many authors and in a variety of scenarios, such as in radiative evaluations [39,40], topological defects solutions [41], supersymmetry [42], Cherenkov radiation [43–45], and classical and quantum aspects [46]. The MCFJ electrodynamics is also relevant due to its connection with the axion Lagrangian [47,48],

$$\mathcal{L} = -\frac{1}{4}F^{\mu\nu}F_{\mu\nu} + \theta(\mathbf{E}\cdot\mathbf{B}), \tag{9}$$

where $F_{\mu\nu} = \partial_\mu A_\nu - \partial_\nu A_\mu$ is the field strength and the axion term, $\theta\tilde{F}^{\alpha\beta}F_{\alpha\beta}$, implies

$$\mathcal{L} = -\frac{1}{4}F^{\mu\nu}F_{\mu\nu} + \frac{1}{4}\epsilon^{\mu\nu\alpha\beta}(\partial_\mu\theta)A_\nu F_{\alpha\beta}. \tag{10}$$

with the dual tensor, $\tilde{F}^{\mu\nu} = (1/2)\epsilon^{\mu\nu\alpha\beta}F_{\alpha\beta}$. In the case where the axion derivative is a constant vector, $\partial_\mu\theta = (k_{AF})_\mu$, the Lagrangian (10) recovers the MCFJ one,

$$\mathcal{L} = -\frac{1}{4}G^{\mu\nu}F_{\mu\nu} + \frac{1}{4}\epsilon^{\mu\nu\alpha\beta}(k_{AF})_\mu A_\nu F_{\alpha\beta} - A_\mu J^\mu, \tag{11}$$

where $(k_{AF})_\mu$ is the LV 4-vector background and $G^{\mu\nu} = \frac{1}{2}\chi^{\mu\nu\alpha\beta}F_{\alpha\beta}$ is the continuous matter field strength.[1] Such a Lagrangian provides the modified electrodynamics in matter, described by the inhomogeneous Maxwell equations,

$$\nabla\cdot\mathbf{D} = J^0 - \mathbf{k}_{AF}\cdot\mathbf{B}, \tag{12}$$

$$\nabla\times\mathbf{H} - \frac{\partial\mathbf{D}}{\partial t} = \mathbf{J} - k_{AF}^0\mathbf{B} + \mathbf{k}_{AF}\times\mathbf{E}, \tag{13}$$

where $G^{i0} = D^i$, $G^{ij} = -\epsilon_{ijk}H^k$, and $(k_{AF})^\mu = (k_{AF}^0, \mathbf{k}_{AF})$. These must be considered together with the homogeneous Maxwell equations, obtained from the Bianchi identity $\partial_\mu\tilde{F}^{\mu\nu} = 0$, and suitable constitutive relations.

The timelike CFJ component, k_{AF}^0, appears in the modified Ampère's law (13) composing the chiral magnetic current,

$$\mathbf{J}_B = k_{AF}^0\mathbf{B}, \tag{14}$$

which has been used to investigate electromagnetic properties of matter endowed with the chiral magnetic effect (CME) [50]. The CME [51,52] consists of a macroscopic

[1]The 4-rank tensor, $\chi^{\mu\nu\alpha\beta}$, describes the medium constitutive tensor [49], whose components provide the electric and magnetic responses of the medium. Indeed, the electric permittivity and magnetic permeability tensor components are written as $\epsilon_{ij} \equiv \chi^{0i j0}$ and $\mu_{lk}^{-1} \equiv \frac{1}{4}\epsilon_{ijl}\chi^{ijmn}\epsilon_{mnk}$, respectively. For isotropic polarization and magnetization, it holds that $\epsilon_{ij} = \epsilon\delta_{ij}$ and $\mu_{ij}^{-1} = \mu^{-1}\delta_{ij}$, providing the usual isotropic constitutive relations, $\mathbf{D} = \epsilon\mathbf{E}$, $\mathbf{H} = \mu^{-1}\mathbf{B}$.

linear magnetic current law, $\mathbf{J} = \sigma_B \mathbf{B}$, stemming from an asymmetry between the number density of left- and right-handed chiral fermions. Such an effect has been investigated in a plethora of distinct contexts [53–58], including Weyl semimetals (WSMs) [59], where the chiral current may be different from the usual CME linear relation when electric and magnetic fields are applied, yielding a current effectively proportional to B^2, that is, $\mathbf{J} = \sigma(\mathbf{E}\cdot\mathbf{B})\mathbf{B}$ [33,60,61].

The spacelike vector, $\mathbf{k}_{AF}$, describes an anomalous charge density in Gauss' law (12) and contributes to the current density,

$$\mathbf{J}_{AH} = \mathbf{k}_{AF} \times \mathbf{E}, \tag{15}$$

in the Ampère's law (13), associated with the anomalous Hall effect (AHE), with $\mathbf{k}_{AF}$ playing the role of anomalous Hall conductivity [50]. The AHE engenders an electric current in the presence of an electric field due to the separation between the energy-crossing points in momentum space for right-handed and left-handed fermions [62–65]. It has been investigated in distinct contexts, such as noncollinear antiferromagnets [66,67], chiral spin liquids [68], and WSMs [69]. Optical effects of a WSM with broken time-reversal and inversion symmetries governed by the axion and the AHE terms were recently examined in WSM systems, with a focus on magneto-optical (Faraday, Kerr, and Voigt) effects [69,70]. The AHE term has also been considered in the propagation of surface plasmon polaritons in WSMs [71]. Optical effects induced by the current term $\mathbf{k}_{AF} \times \mathbf{E}$ were also examined in the context of the MCFJ electrodynamics in continuous media [72]. The anomalous Hall current is also connected with a static axion scenario, $\partial_t \theta = 0$, with a constant gradient $\boldsymbol{\nabla}\theta = cte$, as considered to address an axionic Casimir-like effect in Ref. [73].

In a recent investigation [74], the chiral effects of the CFJ timelike (pseudoscalar) chiral component, k^0_{AF}, on the electromagnetic modes in magnetized cold plasmas were addressed. The electromagnetic and optical properties of the propagating modes, such as birefringence, absorption, and optical rotation, were discussed, with careful comparisons with the usual cold plasma features allowing the identification of the role played by the chiral factor.

In this work, we study wave propagation in a magnetized cold plasma governed by the Maxwell equations (12) and (13) modified by the AHE current term, $\mathbf{J}_{AH} = \mathbf{k}_{AF} \times \mathbf{E}$, which, using the plane-wave ansatz, read

$$i\varepsilon_{ij} k^i E^j + \mathbf{k}_{AF} \cdot \mathbf{B} = 0, \tag{16a}$$

$$i\mathbf{k} \times \mathbf{B} + i\mu_0 \omega \varepsilon_{ij} k^i E^j - \mu_0 \mathbf{k}_{AF} \times \mathbf{E} = 0. \tag{16b}$$

We also consider anisotropic constitutive relations (in the electric polarization sector),

$$D^i = \varepsilon_{ij}(\omega) E^j, \qquad B^i = \mu_0 H^i, \tag{17}$$

where ε_{ij} is the cold plasma permittivity (3) and μ_0 is the vacuum permeability. The modified wave equation for the electric field is

$$M_{ij} E^j = 0, \tag{18}$$

with

$$M_{ij} = n^2 \delta_{ij} - n_i n_j - \frac{\varepsilon_{ij}}{\varepsilon_0} - \frac{i}{\omega} \epsilon_{ikj} V^k, \tag{19}$$

written in terms of the refractive index $\mathbf{n} = \mathbf{k}/\omega$ and with $V^k = k^k_{AF}/\varepsilon_0$ appearing as the redefined components of the chiral vector (which breaks the time-reversal symmetry and preserves space inversion). In this scenario, the wave equation (18) becomes

$$\left[n^2 \delta_{ij} - n^i n^j - \frac{\varepsilon_{ij}}{\varepsilon_0} - i \frac{V^k}{\omega} \epsilon_{ikj} \right] E^j = 0, \tag{20}$$

from which arise the dispersion relations that describe the wave propagation in the medium (by setting $\det M_{ij} = 0$). To obtain the electromagnetic collective modes of a cold plasma modified by the anomalous Hall current–like term, one implements the plasma permittivity tensor (3) in the wave equation (20), yielding the linear homogeneous system

$$\begin{bmatrix} n^2 - n_x^2 - S & -n_x n_y + iD + i(V_z/\omega) & -n_x n_z - i(V_y/\omega) \\ -n_x n_y - iD - i(V_z/\omega) & n^2 - n_y^2 - S & -n_y n_z + i(V_x/\omega) \\ -n_x n_z + i(V_y/\omega) & -n_y n_z - i(V_x/\omega) & n^2 - n_z^2 - P \end{bmatrix} \begin{bmatrix} \delta E_x \\ \delta E_y \\ \delta E_z \end{bmatrix} = 0. \tag{21}$$

The refractive indices and associated propagating modes are also obtained, entailing the examination of the optical effects of birefringence and dichroism. Each scenario is analyzed in the cases of propagation along the magnetic field and orthogonal to the magnetic field, also known as the Faraday and Voigt configurations, respectively [75].

This paper is outlined as follows. In Sec. II we obtain the general dispersion relation for a cold magnetized plasma in

the presence of the anomalous Hall current, considering the Faraday configuration. In Sec. III we discuss the general properties of the cold plasma modes in the Voigt configuration. The dispersion relations, refractive indices, and optical properties, such as birefringence and absorption, are determined in all cases examined. Finally, we summarize our results in Sec. IV.

II. WAVE PROPAGATION ALONG THE MAGNETIC FIELD AXIS

In this section, we analyze the wave propagation along the magnetic field direction, that is, $\mathbf{n} = n\hat{z}$. Then, it holds that

$$\begin{bmatrix} n^2 - S & +iD + i(|\mathbf{V}|/\omega)\cos\beta & -i(|\mathbf{V}|/\omega)\sin\phi\sin\beta \\ -iD - i(|\mathbf{V}|/\omega)\cos\beta & n^2 - S & +i(|\mathbf{V}|/\omega)\sin\beta\cos\phi \\ i(|\mathbf{V}|/\omega)\sin\phi\sin\beta & -i(|\mathbf{V}|/\omega)\sin\beta\cos\phi & -P \end{bmatrix} \begin{bmatrix} \delta E_x \\ \delta E_y \\ \delta E_z \end{bmatrix} = 0, \tag{22}$$

where we have used, without loss of generality, the spherical parametrization

$$\mathbf{V} = |\mathbf{V}|(\sin\beta\cos\phi, \sin\beta\sin\phi, \cos\beta), \tag{23}$$

with the angle β defined between the external magnetic $\mathbf{B}_0$ field and the background vector $\mathbf{V}$. Requiring $\det[M_{ij}] = 0$ in Eq. (22), the dispersion relations are given by

$$2P[D^2 - (n^2 - S)^2] + \frac{|\mathbf{V}|^2}{\omega^2}(P + S - n^2) + \Gamma_\beta = 0, \tag{24}$$

where

$$\Gamma_\beta = \frac{|\mathbf{V}|^2}{\omega^2}\cos(2\beta)(n^2 + P - S) + 4DP\frac{|\mathbf{V}|}{\omega}\cos(\beta). \tag{25}$$

We note that the dispersion relation (24) depends only on the β angle. Thus, we can organize the analysis of the dispersion relation (24) by considering two main scenarios: (i) a chiral vector parallel to the magnetic field and (ii) a chiral vector orthogonal to the magnetic field.

A. Chiral vector parallel to the magnetic field

For a chiral vector parallel to the magnetic field, $\mathbf{V}\|\mathbf{B}$, one sets $\beta \to 0$ in Eq. (24), implying

$$P((n^2 - S)^2 - (D + |\mathbf{V}|/\omega)^2) = 0. \tag{26}$$

Longitudinal waves, with $\mathbf{n}\|\delta\mathbf{E}$ or $\delta\mathbf{E} = (0, 0, \delta E_z)$, may occur when $P = 0$, with nonpropagating vibration at the plasma frequency, $\omega = \omega_p$.

For transverse waves, $\mathbf{n}\perp\delta\mathbf{E}$ or $\delta\mathbf{E} = (\delta E_x, \delta E_y, 0)$, the dispersion relation (26) simplifies to

$$(n^2 - S)^2 - (D + |\mathbf{V}|/\omega)^2 = 0 \tag{27}$$

which, with the relations (4), provides the following refractive indices:

$$(n_R)^2 = 1 - \frac{\omega_p^2}{\omega(\omega - \omega_c)} - \frac{|\mathbf{V}|}{\omega}, \tag{28}$$

$$(n_L)^2 = 1 - \frac{\omega_p^2}{\omega(\omega + \omega_c)} + \frac{|\mathbf{V}|}{\omega}. \tag{29}$$

The indices n_R and n_L may be real or complex in some frequency ranges, enriching their behavior in comparison to the usual cold plasma one. The propagation and absorption zones are modified by the presence of the chiral vector $\mathbf{V}$, as will be shown later.

The propagating modes associated with the refractive indices, given in Eqs. (28) and (29), are obtained as the corresponding eigenvectors (with a null eigenvalue) of Eq. (22). The resulting electric fields are the LCP and RCP modes, namely,

$$n_L \to \mathbf{E}_{\mathrm{LCP}} = \frac{1}{\sqrt{2}}\begin{bmatrix} 1 \\ +i \\ 0 \end{bmatrix}, \tag{30}$$

$$n_R \to \mathbf{E}_{\mathrm{RCP}} = \frac{1}{\sqrt{2}}\begin{bmatrix} 1 \\ -i \\ 0 \end{bmatrix}. \tag{31}$$

There are two cutoff frequencies for the refractive index n_R in (28),

$$\omega_R^{\pm} = \frac{1}{2}((\omega_c + |\mathbf{V}|) \pm \sqrt{(\omega_c - |\mathbf{V}|)^2 + 4\omega_p^2}). \tag{32}$$

While the cutoff frequency ω_R^+ is always positive, ω_R^- is positive only under the condition

$$|\mathbf{V}| > \omega_p^2/\omega_c, \tag{33}$$

for which the index n_R presents two (positive) roots. The refractive index n_L (29) has a single cutoff frequency,

$$\omega_L = -\frac{1}{2}\omega_c - \frac{1}{2}|\mathbf{V}| + \frac{1}{2}\sqrt{(\omega_c - |\mathbf{V}|)^2 + 4\omega_p^2}, \quad (34)$$

which is positive for the condition

$$|\mathbf{V}| < \omega_p^2/\omega_c. \quad (35)$$

To examine the behavior of the refractive indices (28) and (29), we consider two distinct scenarios, following the conditions (33) and (35):

(1) For $|\mathbf{V}| > \omega_p^2/\omega_c$, the index n_L presents no positive root (no cutoff), while the index n_R has two positive roots.
(2) For $|\mathbf{V}| < \omega_p^2/\omega_c$, both indices n_L and n_R have one positive cutoff.

1. About the index n_R

The general behavior of the index n_R is represented in Fig. 1 in terms of the dimensionless parameter ω/ω_c and under the condition (33), as detailed below.

(i) For $\omega \to 0$, $n_R \to +i\infty$, which is complex and divergent in this limit, differing from the behavior of the usual magnetized plasma index n_-, which provides $n \to \infty$ near the origin.
(ii) For $0 < \omega < \omega_R^-$, an absorption zone appears, where $\mathrm{Im}[n_R] \neq 0$. This characteristic does not manifest in the usual cold plasma index n_-, which is real and positive in this range. See the black line in this frequency zone in Fig. 1.
(iii) For $\omega_R^- < \omega < \omega_c$, n_R is real, with $\mathrm{Re}[n_R] > 0$, revealing a propagation zone.
(iv) For $\omega \to \omega_c$, $n_R \to \infty$, a resonance at the cyclotron frequency occurs.

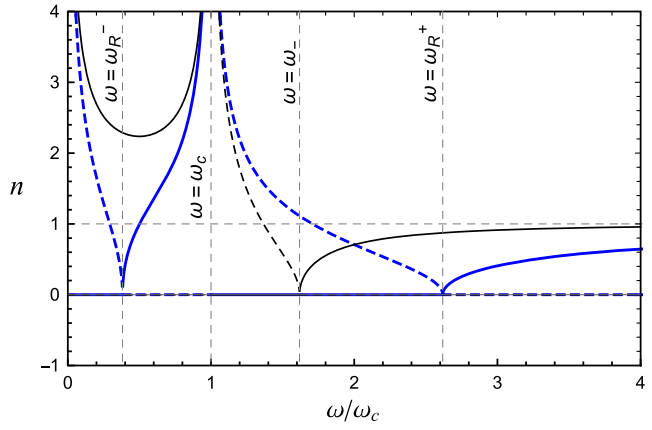

FIG. 1. Index of refraction n_R under the condition (33). The dashed blue (black) line corresponds to the imaginary piece of n_R (n_-), while the solid blue (black) line represents the real piece of n_R (n_-). Note that the chiral factor opens a new lossy window near the origin and enlarges the second absorption zone. Here, $\omega_c = \omega_p$, $|\mathbf{V}| = 2\omega_p$, and $\omega_c = 1$ rad s^{-1}. The (dashed and solid) blue lines representing n_R is thicker than the black line for n_-.

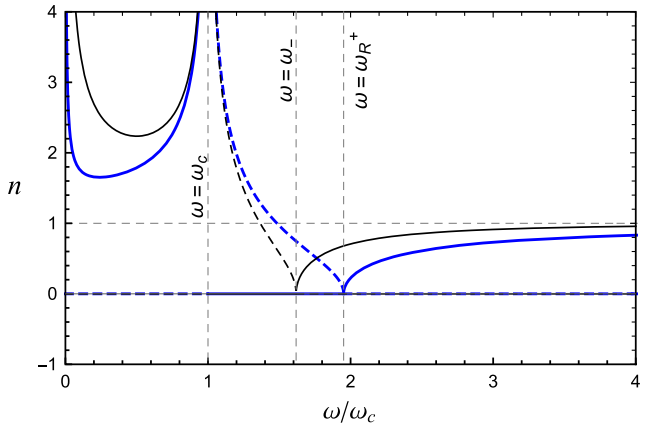

FIG. 2. Index of refraction n_R under the condition (35). The dashed blue (black) line corresponds to the imaginary piece of n_R (n_-), while the solid blue (black) line represents the real piece of n_R (n_-). The chiral factor increases the absorption zone near resonance. Here, $\omega_c = \omega_p$, $|\mathbf{V}| = 0.5\omega_p$, and $\omega_c = 1$ rad s^{-1}. The (dashed and solid) blue lines representing n_R is thicker than the black line for n_-.

(v) For $\omega_c < \omega < \omega_R^+$, there is an absorption zone, where n_R is imaginary, $\mathrm{Im}[n_R] \neq 0$. Such an absorption zone is larger than the usual zone shown by the black-dashed line in Fig. 1, since $\omega_R^+ > \omega_-$.
(vi) For $\omega > \omega_R^+$, the index n_R is real and positive, yielding an attenuation-free propagating zone and recovering $n_R \to 1$ in the high-frequency limit.

On the other hand, under condition (35), $\omega_R^- < 0$, so there is only one cutoff frequency and a single absorption zone, defined for $\omega_c < \omega < \omega_R^+$. The first absorption zone is replaced by a propagation region, now defined for $0 < \omega < \omega_c$, similar to the usual case. For $\omega > \omega_c$, the behavior is similar to that pointed out in items (v) and (vi) above. This scenario for n_R is illustrated in Fig. 2.

2. About the index n_L

The index n_L, given in Eq. (29), has no positive root under the condition (33) (no cutoff frequency) and one cutoff frequency under the condition (35). Its features are described below.

(i) For $\omega \to 0$, under the condition (33), the presence of $|\mathbf{V}|$ renders the refractive index real and positively divergent at the origin, $n_L \to +\infty$, differing from the usual index n_+ (5), which is complex and divergent, $\mathrm{Im}[n_+] \to \infty$, at the origin. This behavior is similar to what is observed in the index n_L of the chiral MCFJ model examined[2] in Ref. [74].
(ii) For $\omega > 0$, the index n_L is always real, $\mathrm{Im}[n_L] = 0$. Thus, wave propagation occurs for any frequency. The real and imaginary parts of n_L are represented in Fig. 3.

[2]See Eq. (48) and Fig. 4 of Ref. [74].

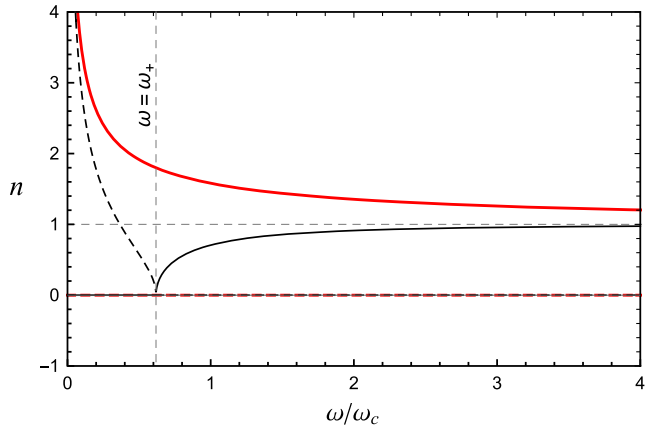

FIG. 3. Refractive index n_L (red lines) for condition (33) and index n_+ (black lines) of Eq. (5). The dashed (solid) lines correspond to the imaginary (real) pieces of n_L and n_+. The chiral factor suppresses the absorption window. Here, $\omega_c = \omega_p$, $|\mathbf{V}| = 2\omega_p$, and $\omega_c = 1\ \mathrm{rad\,s^{-1}}$. The (dashed and solid) red line representing n_L is thicker than the black line for n_+.

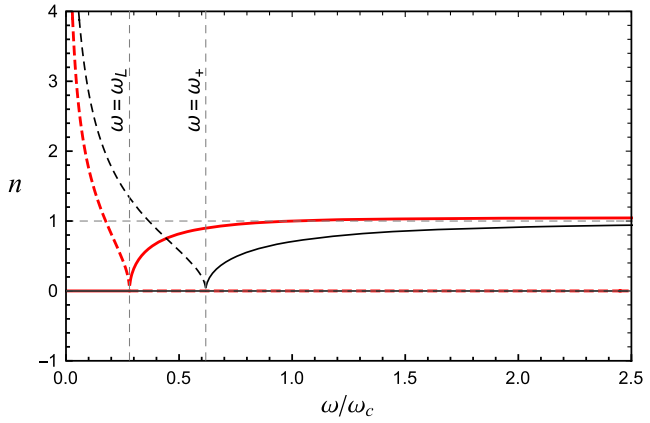

FIG. 4. Refractive index n_L (red lines) for condition (35) and refractive index n_+ (black lines) of Eq. (5). The dashed (solid) lines correspond to the imaginary (real) pieces of n_L and n_+. The chiral factor narrows the absorption zone and enhances the attenuation-free propagation regime. Here, $\omega_c = \omega_p$, $|\mathbf{V}| = 0.5\omega_p$, and $\omega_c = 1\ \mathrm{rad\,s^{-1}}$. The (dashed and solid) red lines representing n_L is thicker than the black line for n_+.

(iii) Under the condition (35), n_L presents a cutoff frequency ω_L, given by Eq. (34). Therefore, an absorption zone appears for $0 < \omega < \omega_L$, where $\mathrm{Im}[n_L] \neq 0$, as depicted in Fig. 4.

We observe that the indices n_R and n_L are always positive, implying the nonexistence of negative refraction, a phenomenon that was reported in the context of the MCFJ cold plasmas in the presence of the chiral timelike background factor.

The results of this subsection may be compared with the case of wave propagation along the magnetic field with the MCFJ timelike background, examined in Sec. IV of Ref [74], whose scenario was richer due to the attainment of four distinct indices and negative refraction, which typically occurs in bi-isotropic media as well [76,77]. In the present case, however, there are only two positive indices (no negative refraction).[3] Nevertheless, regarding the propagation and absorption properties, the present chiral-vector case is more involved since two absorption zones are opened under the condition (33), while in the analogous situation of Ref. [74] only one absorption zone was reported.

3. Dispersion relation behavior

The behavior of the dispersion relations can be visualized in plots of $\omega \times k$. In this subsection, the dispersion relations associated with the circular modes, connected to the indices n_R and n_L, are presented in dimensionless plots of $(\omega/\omega_c) \times (k/\omega_c)$. The dispersion relation associated with $\pm n_R$, under the condition (33), is depicted in Fig. 5. The propagation occurs for $\omega_R^- < \omega < \omega_c$ and $\omega > \omega_R^+$, while two absorption windows appear: $\omega_c < \omega < \omega_R^+$ and $0 < \omega < \omega_R^-$. On the other hand, the behavior for the condition (35) is shown in Fig. 6, where the propagation occurs for $0 < \omega < \omega_c$ and $\omega > \omega_R^+$ and the absorption happens for $\omega_c < \omega < \omega_R^+$. Figures 5 and 6 illustrate

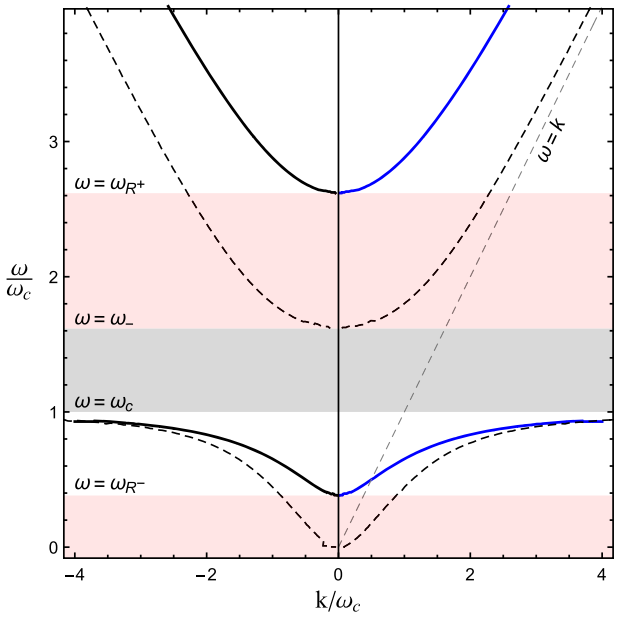

FIG. 5. Dispersion relations related to the refractive indices n_R (solid blue line) and $-n_R$ (solid black line), under the condition (33). The dashed black line represents the indices of the standard case, $\pm n_-$. The highlighted area in red indicates the enlargement of the absorption zone for n_R in comparison to the gray absorption zone of the usual indices ($\pm n_-$). Here we use $\omega_c = \omega_p$ and $|\mathbf{V}| = 2\omega_p$, with $\omega_c = 1\ \mathrm{rad\,s^{-1}}$. Solid blue lines occur for $k/\omega > 0$, and solid black lines for $k/\omega < 0$.

[3]Note that negative indices may also exist in the case where one takes the negative roots of Eqs. (28) and (29), that is, $-n_L$ and $-n_R$, which correspond to the exact mirror image of the positive indices (in relation to the frequency axis).

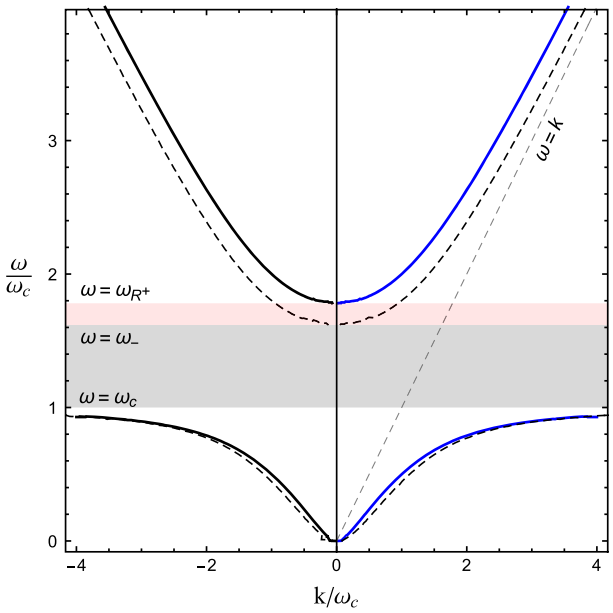

FIG. 6. Plot of the dispersion relations related to the refractive indices n_R (solid blue line) and $-n_R$ (solid black line), under the condition (35). The dashed black line corresponds to the indices of the usual case ($\pm n_-$). The highlighted area in red indicates the absorption zone amplification for n_R in comparison with the one of $\pm n_-$. Here we use $\omega_c = \omega_p$ and $|\mathbf{V}| = 0.5\omega_p$, with $\omega_c = 1\ \mathrm{rad\,s^{-1}}$. Solid blue lines occur for $k/\omega > 0$, and solid black lines for $k/\omega < 0$.

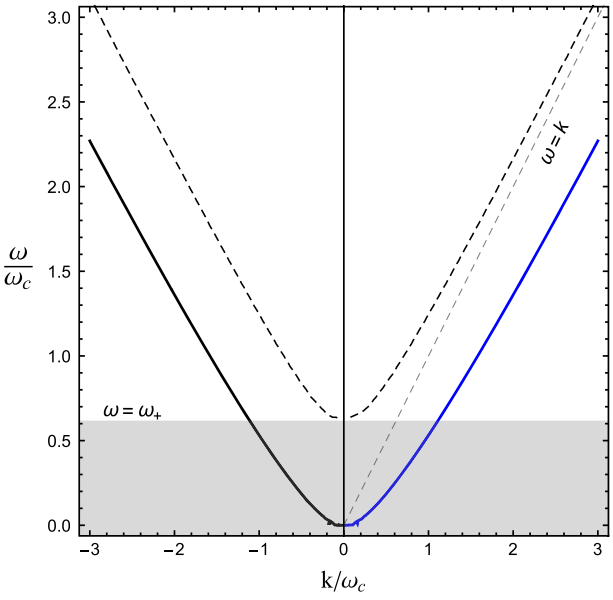

FIG. 7. Dispersion relations associated with the refractive indices n_L (solid blue line) and $-n_L$ (solid black line), under the condition (33). The dashed black line corresponds to the indices of the usual case ($\pm n_+$). The highlighted area in gray indicates the absorption zone for the indices $\pm n_+$, where one notices the absence of absorption for n_L. Here we use $\omega_c = \omega_p$ and $|\mathbf{V}| = 2\omega_p$, with $\omega_c = 1\ \mathrm{rad\,s^{-1}}$. Solid blue lines occur for $k/\omega > 0$, and solid black lines for $k/\omega < 0$.

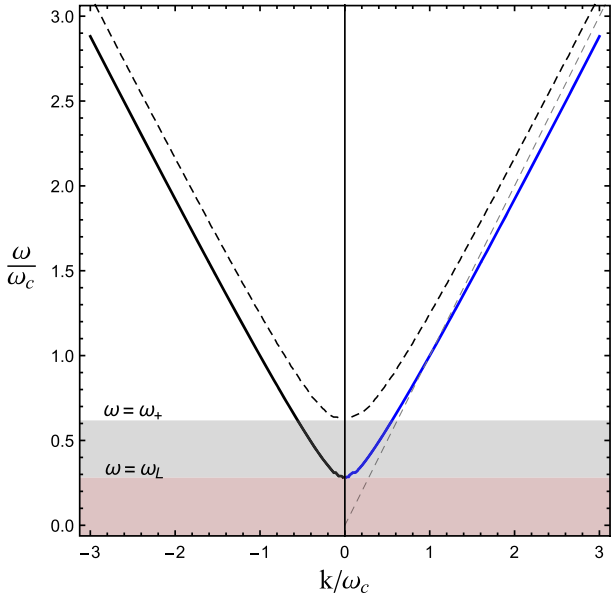

FIG. 8. Dispersion relations associated with the refractive indices n_L (solid blue line) and $-n_L$ (solid black line), under the condition (35). The dashed black line corresponds to the indices of the usual case ($\pm n_+$). The highlighted area in red indicates the absorption zone for n_L, narrowed in comparison to the absorption zone associated with $\pm n_+$. Here we use $\omega_c = \omega_p$ and $|\mathbf{V}| = 0.5\omega_p$, with $\omega_c = 1\ \mathrm{rad\,s^{-1}}$. Solid blue lines occur for $k/\omega > 0$, and solid black lines for $k/\omega < 0$.

enhanced absorption zones. Figure 7 illustrates the dispersion relations associated with $\pm n_L$ for the condition (33), where the propagation occurs for $\omega > 0$, being compatible with the absence of an absorption zone; see Fig. 3. The dispersion relation for the condition (35) is depicted in Fig. 8, where there is an unusual absorption zone in $0 < \omega < \omega_L$, while the propagation appears for $\omega > \omega_L$. In these two latter cases, the absorption zone is reduced in comparison to the zone of the usual indices, $\pm n_+$, $0 < \omega < \omega_+$.

An interesting point is that the refractive indices $n_{R,L}$, represented by blue lines in Figs. 5–8, do not become negative under the influence of the chiral vector $\mathbf{V}$, allowing the plots of $\omega \times k$ to remain centered at $k = 0$. This is not the case for cold plasmas under the timelike CFJ electrodynamics [74], where the scalar chiral parameter V_0 induces zones of negative refraction (negative refractive indices), decentralizing the curves of $\omega \times k$ (see Ref. [74]).

4. Low-frequency helicon modes

There are low-frequency plasma modes that propagate along the magnetic field axis, called helicons. In a usual magnetized plasma, there exist only RCP helicon modes,[4] for which the refractive index (5) yields

[4]See Chapter 9 of Ref. [10] and Chapter 8 of Ref. [3] for basic details.

$$n_- = \omega_p \sqrt{\frac{1}{\omega\omega_c}} \tag{36}$$

in the low-frequency regime,

$$\omega \ll \omega_p, \qquad \omega_c \ll \omega_p, \qquad \omega \ll \omega_c. \tag{37}$$

Considering the circular electromagnetic modes associated with the indices (28) and (29), the corresponding helicons indices are

$$\bar{n}_R = \sqrt{\frac{\omega_p^2}{\omega\omega_c} - \frac{|\mathbf{V}|}{\omega}}, \tag{38a}$$

$$\bar{n}_L = \sqrt{\frac{|\mathbf{V}|}{\omega} - \frac{\omega_p^2}{\omega\omega_c}}, \tag{38b}$$

where we have used the "bar" notation to indicate the helicons quantities. Due to the chiral vector $|\mathbf{V}|$, one obtains expressions for both RCP and LCP helicons. As $\bar{n}_R^2 = -\bar{n}_L^2$, one of these indices is imaginary when the other is real. In fact, $\bar{n}_R$ becomes imaginary for $|\mathbf{V}| > \omega_p^2/\omega_c$, while $\bar{n}_L$ is imaginary for $|\mathbf{V}| < \omega_p^2/\omega_c$. This means that RCP and LCP helicons do not propagate simultaneously. Indeed, only one of the modes in Eq. (38) can propagate for each value of $|\mathbf{V}|$ adopted. In this context, note that the usual cold plasma helicon mode is recovered in the limit $|\mathbf{V}| \to 0$, for which the helicon index $\bar{n}_R$ yields the usual result of Eq. (36), while $\bar{n}_L$ becomes purely imaginary, indicating the absence of propagation.

5. Rotatory power

Chiral media possess optical activity, described in terms of the rotation of the polarization (birefringence) that takes place when RCP and LCP modes propagate at different phase velocities. Such a rotation is measured in terms of the rotatory power, which is useful for performing an optical characterization of multiple systems, such as crystals [78,79], organic compounds [80,81], graphene phenomena in the terahertz band [82], the gas of fast-spinning molecules [83], chiral metamaterials [84–86], and chiral semimetals [87,88], and in the determination of the rotation direction of pulsars [89]. The RP may be dispersive (depend on the frequency) [90–92]. The RP is defined as

$$\delta = -\frac{\omega}{2}(\mathrm{Re}[n_L] - \mathrm{Re}[n_R]), \tag{39}$$

where n_L and n_R are the refractive indices for different circular polarizations. For the case where the background vector is parallel to the magnetic field (see Sec. II A), the refractive indices, given by Eqs. (28) and (29), yield

$$\delta = -\frac{\omega}{2}\mathrm{Re}\left[\sqrt{R_+} - \sqrt{R_-}\right], \tag{40}$$

where $R_\pm$ is given by

$$R_\pm = 1 - \frac{\omega_p^2}{\omega(\omega \pm \omega_c)} \pm \frac{|\mathbf{V}|}{\omega}. \tag{41}$$

The behavior of the RP (40) is depicted in Fig. 9, being negative for the interval $0 < \omega < \hat{\omega}$ and positive for $\hat{\omega} < \omega < \omega_c$. For $\omega > \omega_c$, the RP is always negative, exhibiting a sharp behavior at $\omega = \omega_R$, the point at which the real piece of n_R assumes nonzero values again (see Fig. 1). The frequency $\hat{\omega}$,

$$\hat{\omega} = \sqrt{\omega_c(\omega_c - \omega_p^2/|\mathbf{V}|)}, \tag{42}$$

obtained from Eqs. (40) and (41), indicates where the RP changes sign, as shown in Fig. 9. Note that $\hat{\omega}$ is real only for the condition (33). Hence, the RP reversion only occurs in this case, as confirmed in Fig. 9. In fact, under the condition (35), the corresponding RP depicted in Fig. 10 is not endowed with sign reversal, a behavior analog to the standard RP in plasmas.

It is worth remarking that the RP reversion is observed in graphene systems [82], Weyl metals and semimetals with low electron density with chiral conductivity [87,88], and bi-isotropic dielectrics with magnetic chiral conductivity [93]. Such a reversion does not occur in conventional cold plasma, but it takes place in rotating plasmas [94] and in the MCFJ plasma with a chiral pseudoscalar factor [74]. Therefore, RP reversion may be considered a signature of chiral MCFJ nonrotating cold plasmas.

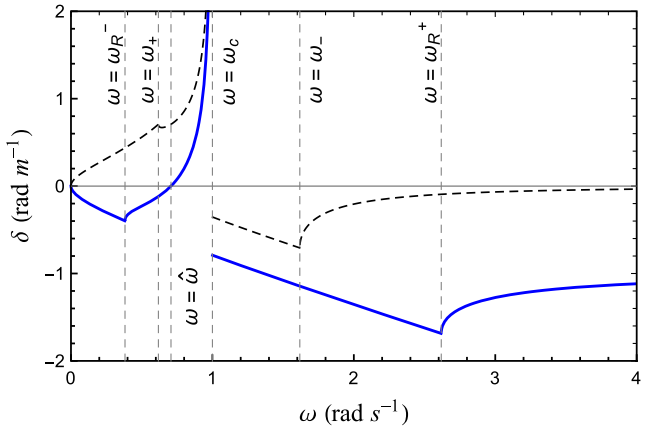

FIG. 9. The solid blue line represents the RP (40) defined by the refractive index n_L and n_R for the condition (33). The dashed black line corresponds to the usual RP for a conventional cold plasma. The chiral factor determines the RP sign reversion at $\omega < \hat{\omega}$ and a constant asymptotic value, $-|\mathbf{V}|/2$, for high frequencies. Here we use $\omega_c = \omega_p$, $|\mathbf{V}| = 2\omega_p$, and $\omega_c = 1\ \mathrm{rad\,s^{-1}}$.

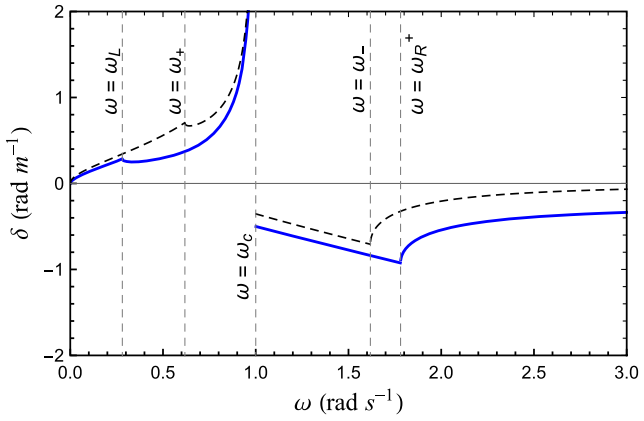

FIG. 10. Solid blue lines: RP (40) associated with the refractive indices n_L and n_R for the condition (35). The dashed line represents the usual RP for a usual cold plasma. Small deviations of the RP are originated from the chiral factor. The main difference in comparison with the usual case is the non-null asymptotical value, $-|\mathbf{V}|/2$, for high frequencies. Here we use $\omega_c = \omega_p$, $|\mathbf{V}| = 0.5\omega_p$, and $\omega_c = 1$ rad s^{-1}.

Furthermore, it is important to pay attention to the intervals $0 < \omega < \omega_R^-$ and $\omega_c < \omega < \omega_R^+$, where the refractive index n_R is imaginary and the RP receives a contribution only from the index n_L, exhibiting an approximately linearly increasing magnitude, the opposite of the n_L profile. For $\omega > \omega_R^+$, the modes associated with the n_L and n_R propagate and contribute to the RP, whose magnitude diminishes monotonically with ω, tending to the asymptotic value $-|\mathbf{V}|/2$, as shown in Fig. 9. In fact, in the high-frequency limit, $\omega \gg \omega_p, \omega_c$, the refractive indices n_L and n_R provide (at first order)

$$n_{L,R} \simeq 1 \pm \frac{|\mathbf{V}|}{2\omega}, \tag{43}$$

so the RP asymptotic value is

$$\delta \simeq -\frac{|\mathbf{V}|}{2}, \tag{44}$$

a result that holds even in the absence of the magnetic field. This asymptotic limit differs from the behavior of a cold usual plasma, whose RP decays as $1/\omega^2$ for high frequencies, tending to zero for $\omega \gg \omega_p, \omega_c$. See the dashed line in Fig. 9.

6. Dichroism coefficients

Absorption occurs in the zones where the indices are complex. When circularly polarized modes undergo absorption at different degrees, dichroism takes place, working as another parameter for optical characterization. It could be used to distinguish between Dirac and Weyl semimetals [95], perform enantiomeric discrimination [96,97], and develop graphene-based devices at terahertz frequencies [98]. Dichroism for LCP and RCP waves is expressed in terms of the coefficient

$$\delta_d = -\frac{\omega}{2}(\mathrm{Im}[n_L] - \mathrm{Im}[n_R]). \tag{45}$$

For the condition (33), n_R has non-null imaginary parts in the intervals $0 < \omega < \omega_R^-$ and $\omega_c < \omega < \omega_R^+$, while n_L is always real (for $\omega > 0$). In this case, the dichroism coefficient is written as

$$\delta_d = \begin{cases} \frac{\omega}{2}\sqrt{R_-}, & \text{for } 0 < \omega < \omega_R^-, \\ 0, & \text{for } \omega_R^- < \omega < \omega_c, \\ \frac{\omega}{2}\sqrt{R_-}, & \text{for } \omega_c < \omega < \omega_R^+, \\ 0, & \text{for } \omega > \omega_R^+, \end{cases} \tag{46}$$

with R_- of Eq. (41). Such a coefficient is depicted in Fig. 11.

Considering the condition (35), both n_R and n_L have non-null imaginary parts in the intervals $\omega_c < \omega < \omega_R^+$ and $0 < \omega < \omega_L$, respectively, in which the dichroism coefficient is non-null,

$$\delta_d = \begin{cases} -\frac{\omega}{2}\sqrt{R_+}, & \text{for } 0 < \omega < \omega_L, \\ +\frac{\omega}{2}\sqrt{R_-}, & \text{for } \omega_c < \omega < \omega_R^+. \end{cases} \tag{47}$$

The general behavior of (47) is exhibited in Fig. 12.

B. Chiral vector orthogonal to the magnetic field

In the scenario where the background vector is orthogonal to the magnetic field, $\beta \to \pi/2$, and the dispersion relation (24) reads

$$P[D^2 - (n^2 - S)^2] + (|\mathbf{V}|^2/\omega^2)(S - n^2) = 0, \tag{48}$$

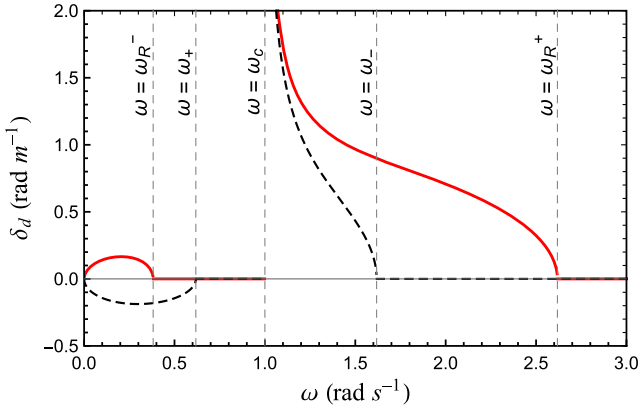

FIG. 11. Dichroism coefficient of Eq. (46) (red solid lines) associated with n_L and n_R, under the condition (33). The black dashed line represents the dichroism coefficient of a usual cold plasma. Here, $\omega_c = \omega_p$, $|\mathbf{V}| = 2\omega_p$, and $\omega_c = 1$ rad s^{-1}.

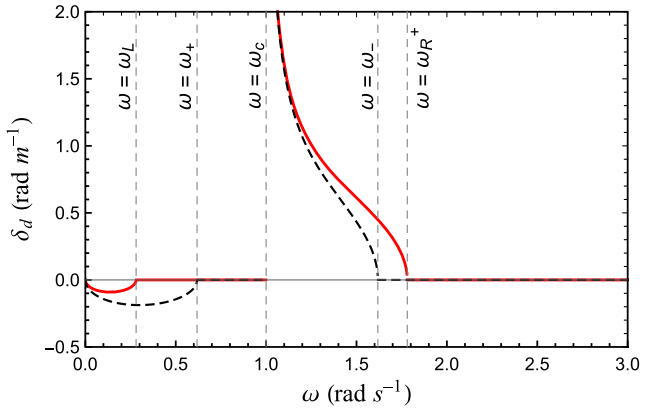

FIG. 12. Dichroism coefficient of Eq. (47) (solid red lines) associated with n_L and n_R, under the condition (35). The dashed line represents the dichroism coefficient for a conventional cold plasma. Here, we set $\omega_c = \omega_p$, $|\mathbf{V}| = 0.5\omega_p$, and $\omega_c = 1$ rad s^{-1}.

yielding two refractive indices:

$$(n_A)^2 = S - \frac{|\mathbf{V}|^2}{2P\omega^2} + \frac{1}{P}\sqrt{P^2D^2 + \frac{|\mathbf{V}|^4}{4\omega^4}}, \tag{49}$$

$$(n_B)^2 = S - \frac{|\mathbf{V}|^2}{2P\omega^2} - \frac{1}{P}\sqrt{P^2D^2 + \frac{|\mathbf{V}|^4}{4\omega^4}}. \tag{50}$$

From Eq. (22), mixed elliptical polarizations are evaluated for the propagating modes,

$$n_{A,B} \to \mathbf{E}_{A,B} = C\begin{bmatrix} -\zeta \\ 1 \\ -i|\mathbf{V}|(n_{A,B}^2 - S)/(\omega\bar{\kappa}P) \end{bmatrix}, \tag{51a}$$

where

$$C = \frac{|\bar{\kappa}|}{\sqrt{(n^2-S)^2[(|\mathbf{V}|/\omega P)^2 + \sin^2\phi] + D^2\cos^2\phi + |\bar{\kappa}|^2}}, \tag{51b}$$

$$\zeta = \frac{((n^2-S)^2 - D^2)\cos\phi\sin\phi + iD(n^2-S)}{|\bar{\kappa}|^2}, \tag{51c}$$

$$\bar{\kappa} = (n^2 - S)\cos\phi - iD\sin\phi. \tag{51d}$$

In Eq. (51a), one notices a longitudinal imaginary component. The transversal sector is, in general, elliptically polarized since ζ is a complex quantity. Starting from Eq. (51a) and setting $|\mathbf{V}| \to 0$, the usual RCP and LCP modes are recovered, which is an expected correspondence.

The refractive indices given in (49) and (50) have real positive roots given by

$$\omega_{A1,B} = \frac{1}{6}\sqrt{8\omega_c^2 \mp 2\sqrt[3]{\frac{\mp 2}{U}}f_1 + (\mp 2)^{2/3}\sqrt[3]{U} + 2|\mathbf{V}|^2}, \tag{52}$$

$$\omega_{A2} = \frac{1}{6}\sqrt{8\omega_c^2 + \frac{(2)^{4/3}(-1)^{2/3}f_1}{\sqrt[3]{U}} - f_4}, \tag{53}$$

where

$$U = 11\omega_c^6 + f_2 + 3\sqrt{3}\sqrt{-c^4(5\omega_c^8 + f_3)}, \tag{54a}$$

$$f_1 = 4\omega_c^4 + 2\omega_c^2|\mathbf{V}|^2 + |\mathbf{V}|^4, \tag{54b}$$

$$f_2 = -12\omega_c^4|\mathbf{V}|^2 + 6\omega_c^2|\mathbf{V}|^4 + 2|\mathbf{V}|^6, \tag{54c}$$

$$f_3 = 24\omega_c^6|\mathbf{V}|^2 + 4\omega_c^4|\mathbf{V}|^4 + 12\omega_c^2|\mathbf{V}|^6 + 4|\mathbf{V}|^8, \tag{54d}$$

$$f_4 = \sqrt{3} - 1(2)^{2/3}\sqrt[3]{U} + 2|\mathbf{V}|^2, \tag{54e}$$

where $\omega_{A1,2}$ is associated with n_A and ω_B is associated with n_B.

1. About the index n_A

The refractive index n_A, given in Eq. (49), has two positive roots, ω_{A1} and ω_{A2}, as illustrated in Fig. 13, where we observe the following:

(i) For $\omega \to 0$, the index is imaginary and tends to infinity, $n_A \to +i\infty$, which is the same behavior as for the usual magnetized plasma index n_+ near the origin.

(ii) For $0 < \omega < \omega_{A1}$, it holds that $\mathrm{Re}[n_A] = 0$, $\mathrm{Im}[n_A] \neq 0$, defining an absorption zone.

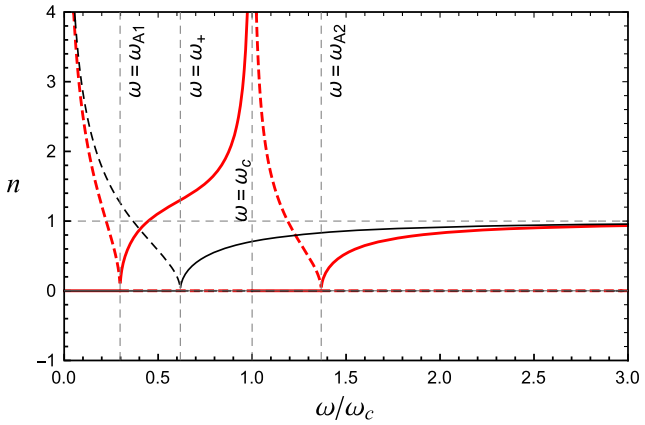

FIG. 13. Refractive index n_A (red lines) and n_+ (black lines) of Eq. (5). The dashed (solid) lines correspond to the imaginary (real) pieces of n_A and n_+. There is an intermediary propagation zone in the range $\omega_{A1} < \omega < \omega_c$ and a new absorption interval defined for $\omega_c < \omega < \omega_{A2}$. Here, $\omega_c = \omega_p$, $|\mathbf{V}| = 2\omega_p$, and $\omega_c = 1$ rad s^{-1}. The (solid and dashed) red curves are thicker than the (solid and dashed) black lines.

(iii) For $\omega_{A1} < \omega < \omega_c$, n_A is real, $\mathrm{Re}[n_A] > 0$ and $\mathrm{Im}[n_A] = 0$, opening an intermediary propagation zone that does not appear in the usual case. Compare the black and red lines in Fig. 13.

(iv) For $\omega \to \omega_c$, there is a resonance, $n_A \to \infty$, at the cyclotron frequency, a behavior that is not seen in the standard case. For $\omega_c < \omega < \omega_{A2}$, n_A is imaginary, that is, $\mathrm{Im}[n_A] \neq 0$, $\mathrm{Re}[n_A] = 0$, and thus another absorption zone is allowed.

(v) For $\omega > \omega_{A2}$, there is a propagating zone, in which the index n_A is always positive and real, with $n_A \to 1$ in the high-frequency limit. See Fig. 13.

2. About the index n_B

The index n_B in Eq. (50) has only one cutoff frequency, represented by ω_B. Its real and imaginary parts are illustrated in Fig. 14.

(i) In the limit $\omega \to 0$, the index n_B is real and tends to infinity, $n_B \to +\infty$. For $0 < \omega < \omega_c$, the index n_B is real, with $\mathrm{Im}[n_B] = 0$, a behavior close to that of standard magnetized plasmas.

(ii) For $\omega \to \omega_c$, $n_B \to \infty$, and there is a resonance at the cyclotron frequency. This behavior also occurs in the usual case. For $\omega_c < \omega < \omega_B$, the index is imaginary, $\mathrm{Re}[n_B] = 0$, $\mathrm{Im}[n_B] \neq 0$, describing an absorption zone that is larger than the usual one, since $\omega_B > \omega_-$. See Fig. 14.

(iii) For $\omega > \omega_B$, one has a propagating zone, where n_B is always real and positive, with $n_B \to 1$ in the high-frequency limit.

The results of the present section cannot be compared with those of Ref. [74] since the defining condition of this section—a chiral vector orthogonal to the magnetic field—is not possible in the scenario of a scalar chiral factor [74].

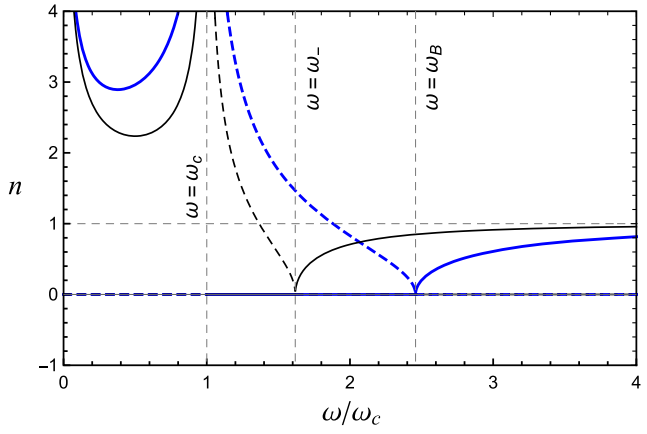

FIG. 14. Refractive index n_B (blue lines) and n_- (black lines) of Eq. (5). The dashed (solid) lines correspond to the imaginary (real) pieces of n_B and n_-. The intermediary absorption zone, $\omega_c < \omega < \omega_B$, has now amplified length. Here, $\omega_c = \omega_p$, $|\mathbf{V}| = 2\omega_p$, and $\omega_c = 1\ \mathrm{rad\,s^{-1}}$. The (solid and dashed) blue curves are thicker than the (solid and dashed) black lines.

3. Optical effects

Considering the configuration of the background vector orthogonal to the magnetic field, the refractive indices (49) and (50) are not associated with circularly polarized modes [see Eq. (51a)]. In this panorama, the birefringence is better characterized in terms of the phase shift per unit length, given by

$$\frac{\Delta}{d} = \frac{2\pi}{\lambda_0}(\mathrm{Re}[n_A] - \mathrm{Re}[n_B]), \tag{55}$$

or, explicitly,

$$\frac{\Delta}{d} = \frac{2\pi}{\lambda_0}\left(\sqrt{S - \frac{|\mathbf{V}|^2}{2P\omega^2} + \Xi_{AB}} - \sqrt{S - \frac{|\mathbf{V}|^2}{2P\omega^2} - \Xi_{AB}}\right), \tag{56}$$

where

$$\Xi_{AB}(\omega, |\mathbf{V}|) = \sqrt{D^2 + \frac{|\mathbf{V}|^4}{4P^2\omega^4}}. \tag{57}$$

In the high-frequency limit $\omega \gg (\omega_c, \omega_p)$, the phase shift is

$$\frac{\Delta}{d} \simeq -\frac{2\pi}{\lambda_0}\sqrt{\frac{2\omega_c\omega_p^2}{(2\omega^2 - |\mathbf{V}|^2)\omega}}. \tag{58}$$

As for the absorption effect for noncircularly propagating modes, one can define the difference of absorption between the two modes per unit length, written as

$$\frac{\Delta_{\mathrm{Im}}}{d} = \frac{2\pi}{\lambda_0}(\mathrm{Im}[n_A] - \mathrm{Im}[n_B]). \tag{59}$$

For $\omega_c < \omega < \omega_{A2}$, the indices n_A and n_B are purely imaginary; see the corresponding dashed lines in Fig. 13 and 14. In this range, the absorption factor (59) is

$$\frac{\Delta_{\mathrm{Im}}}{d} = \frac{2\pi}{\lambda_0}\left[\sqrt{\frac{|\mathbf{V}|^2}{2P\omega^2} - \Xi_{AB} - S} - \sqrt{\frac{|\mathbf{V}|^2}{2P\omega^2} + \Xi_{AB} - S}\right]. \tag{60}$$

For $\omega < \omega_{A1}$, only the mode associated with n_A is absorbed. In this case, we can write the absorption coefficient $\gamma = 2\omega\mathrm{Im}[n]$, which is explicitly given by

$$\gamma = 2\omega\sqrt{\frac{|\mathbf{V}|^2}{2P\omega^2} - \Xi_{AB} - S}. \tag{61}$$

III. WAVE PROPAGATION ORTHOGONAL TO THE MAGNETIC FIELD

For propagation orthogonal to the magnetic field, we can implement $\mathbf{n} = (n_x, n_y, 0)$ in Eq. (21). Furthermore, we propose a parametrization for the wave propagation in the plane orthogonal to the magnetic field in terms of the angle α between the propagation direction and the x axis,

$$\mathbf{n} = n(\cos\alpha, \sin\alpha, 0). \tag{62}$$

Thus, Eq. (20) now reads

$$\begin{bmatrix} n^2 - n^2\cos^2\alpha - S & -n^2\cos\alpha\sin\alpha + iD + i(|\mathbf{V}|/\omega)\cos\beta & -i(|\mathbf{V}|/\omega)\sin\phi\sin\beta \\ -n^2\cos\alpha\sin\alpha - iD - i(|\mathbf{V}|/\omega)\cos\beta & n^2 - n^2\sin^2\alpha - S & +i(|\mathbf{V}|/\omega)\cos\phi\sin\beta \\ +i(|\mathbf{V}|/\omega)\sin\phi\sin\beta & -i(|\mathbf{V}|/\omega)\cos\phi\sin\beta & n^2 - P \end{bmatrix} \begin{bmatrix} \delta E_x \\ \delta E_y \\ \delta E_z \end{bmatrix} = 0. \tag{63}$$

The null determinant condition provides the following dispersion relation:

$$(n^2 - P)[D^2 + S(n^2 - S))] - (|\mathbf{V}|/2\omega)^2\Theta = 0, \tag{64}$$

where

$$\Theta = [2(P+S) - 3n^2] + 8D\omega(P - n^2)\cos\beta/|\mathbf{V}| - (n^2 - 2P + 2S)\cos(2\beta) + 2n^2\sin^2(\beta)\cos(2(\alpha - \phi)). \tag{65}$$

A. Chiral vector parallel to the magnetic field

A chiral vector parallel to the magnetic field, $\mathbf{V}\|\mathbf{B_0}$, implies $\beta = 0$, whose replacement in Eq. (64) yields the index n_T^2,

$$n_T^2 = 1 - \frac{\omega_p^2}{\omega^2}, \tag{66}$$

which is also given in Eq. (7) and is associated with the same usual linear transversal mode.

It also provides a modified refractive index,

$$n_\chi^2 = \frac{S^2 - D^2}{S} - \frac{|\mathbf{V}|^2 + 2D|\mathbf{V}|\omega}{S\omega^2}, \tag{67}$$

associated with the elliptical propagating mode,

$$n_\chi \to \mathbf{E} = C_\chi \begin{bmatrix} -\zeta_\chi \\ 1 \\ 0 \end{bmatrix}, \tag{68}$$

where

$$C_\chi = \frac{1}{\sqrt{|\zeta_\chi|^2 + 1}}, \tag{69a}$$

$$\zeta_\chi = \frac{i[D + (|\mathbf{V}|/\omega)] - n^2\cos\alpha\sin\alpha}{n^2\sin^2\alpha - S}. \tag{69b}$$

The refractive index n_χ has three cutoff frequencies, $\omega_R^\pm$ and ω_L, given in Eqs. (32) and (34).

1. About the index n_χ

The refractive index n_χ has the refractive index n_O as the conventional cold plasma counterpart, given in (8), sharing with it the same resonance frequency

$$\omega_{cp} = \sqrt{\omega_c^2 + \omega_p^2}. \tag{70}$$

Under the condition (35), n_χ shows two cutoff frequencies, ω_R^+ and ω_L, which are the same as those of Eqs. (32) and (34), respectively. These frequencies are marked in Fig. 15. Moreover, we point out the following:

(i) For $0 < \omega < \omega_L$, n_χ is imaginary, corresponding to an absorption zone smaller than the usual one,

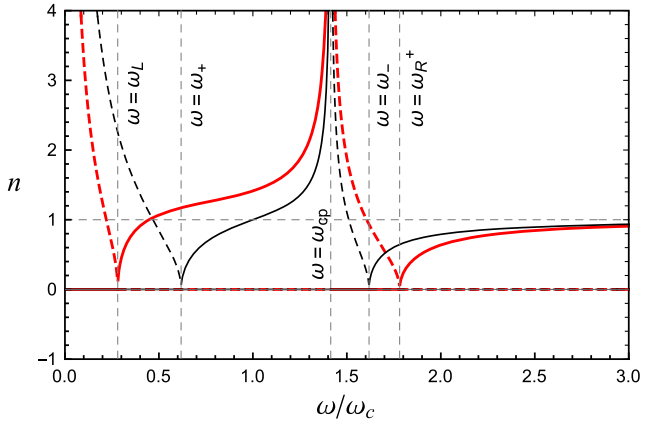

FIG. 15. Red line: index n_χ under the condition (35). Black line: index n_O. Dashed (solid) lines represent the imaginary (real) pieces of n_χ and n_O. Note that the chiral vector factor shortens the first absorption zone and slightly augments the second one. Here we use: $\omega_c = \omega_p$, $|\mathbf{V}| = 0.5\omega_p$, and $\omega_c = 1$ rad s^{-1}. The (solid and dashed) red curves are thicker than the (solid and dashed) black lines.

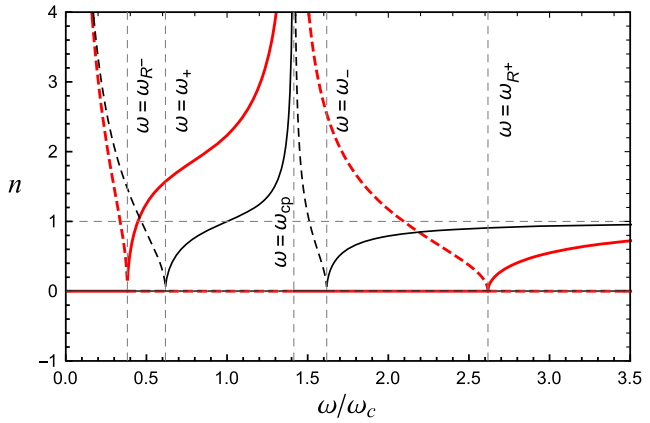

FIG. 16. Red line: plot of the index n_χ under the condition (33). Black line: plot of the index n_O. Dashed (solid) lines represent the imaginary (real) pieces of n_χ and n_O. The chiral vector reduces the first absorption frequency window and enhances the second one. Here we use: $\omega_c = \omega_p$, $|\mathbf{V}| = 2\omega_p$, and $\omega_c = 1$ rad s^{-1}. The (solid and dashed) red curves are thicker than the (solid and dashed) black lines.

$0 < \omega < \omega_+$, since $\omega_L < \omega_+$. See the black dashed line in Fig. 15.

(ii) For $\omega_L < \omega < \omega_{cp}$, $\mathrm{Re}[n_\chi] \neq 0$ and $\mathrm{Im}[n_\chi] = 0$, defining a propagation zone larger than the standard-case one ($\omega_+ < \omega < \omega_{cp}$).

(iii) For $\omega \to \omega_{cp}$, there is a resonance, $n_\chi \to +\infty$, which is the same behavior as in the usual case. For $\omega_{cp} < \omega < \omega_R^+$, $\mathrm{Re}[n_\chi] = 0$ and $\mathrm{Im}[n_\chi] \neq 0$, and another absorption zone is allowed.

(iv) For $\omega > \omega_R^+$, the quantity n_χ is always positive, corresponding to a propagation zone, which in the usual case begins at $\omega = \omega_-$.

Under the condition (33), n_χ has two roots, $\omega_R^\pm$, and similar characteristics to those described above, as shown in Fig. 16.

2. Optical effects

For the configuration of a background vector parallel to the magnetic field, the propagating modes obtained were described by elliptical and linear polarized vectors, associated with the refractive indices n_T and n_χ, respectively. In this case, the birefringence is evaluated by employing the phase shift per unit length,

$$\frac{\Delta}{d} = \frac{2\pi}{\lambda_0}(\mathrm{Re}[n_T] - \mathrm{Re}[n_\chi]), \tag{71}$$

which for the indices (66) and (67) reads

$$\frac{\Delta}{d} = \frac{2\pi}{\lambda_0}\left(\sqrt{P} - \sqrt{\frac{S^2 - D^2}{S} - \frac{|\mathbf{V}|^2 + 2D|\mathbf{V}|\omega}{S\omega^2}}\right). \tag{72}$$

In the limit $\omega \gg (\omega_p, \omega_c)$, using the parameters S, D, and P given in (4), such a phase shift reduces to

$$\frac{\Delta}{d} = \frac{2\pi}{\lambda_0}\left(1 - \sqrt{\frac{\omega^2 - |\mathbf{V}|^2}{\omega^2}}\right). \tag{73}$$

In the usual case, where $\Delta/d \propto (n_T - n_O)$, the phase shift is null in the high-frequency limit, a result recovered for $|\mathbf{V}| \to 0$ in (73). Thus, the chiral vector is responsible for an unusual dispersive birefringence in the high-frequency domain.

Concerning the absorption for noncircularly propagating modes, the difference in absorption between the two modes per unit length,

$$\frac{\Delta_{\mathrm{Im}}}{d} = \frac{2\pi}{\lambda_0}(\mathrm{Im}[n_T] - \mathrm{Im}[n_\chi]), \tag{74}$$

yields

$$\frac{\Delta_{\mathrm{Im}}}{d} = \frac{2\pi}{\lambda_0}\left(\sqrt{P} - \sqrt{\frac{|\mathbf{V}|^2 + 2D|\mathbf{V}|\omega}{S\omega^2} - \frac{S^2 - D^2}{S}}\right) \tag{75}$$

for the indices in Eqs. (66) and (67). It is non-null for $0 < \omega < \omega_{L,R^-}$ and $\omega_{cp} < \omega < \omega_{R^+}$, under the condition (33) or (35), as shown in Figs. 15 and 16, respectively.

B. Background vector orthogonal to the magnetic field

Considering the chiral vector orthogonal to the magnetic field, $\mathbf{V} \perp \mathbf{B}_0$, we take $\beta \to \pi/2$ in Eq. (64), yielding two refractive indices,

$$(n_\Upsilon^2)_\pm = \frac{S(P+S) - D^2}{2S} - \frac{|\mathbf{V}|^2 \sin^2(\alpha - \phi)}{2S\omega^2} \pm \frac{\eta}{4S\omega^2}, \tag{76}$$

where

$$\eta = \sqrt{\Lambda^2 - 16S\omega^2(P\omega^2(S^2 - D^2) - S|\mathbf{V}|^2)}, \tag{77a}$$

$$\Lambda = 2(D^2 - S^2 - PS)\omega^2 - |\mathbf{V}|^2\cos(2(\alpha - \phi)) + |\mathbf{V}|^2. \tag{77b}$$

The indices $(n_\Upsilon^2)_\pm$ are related to the following electromagnetic modes:

$$(n_\Upsilon)_\pm \to \mathbf{E}_\pm = C_\Upsilon \begin{bmatrix} -\zeta_\Upsilon \\ 1 \\ \frac{|\mathbf{V}|(\cos\phi + i\zeta_\Upsilon \sin\phi)}{\omega(n_\pm^2 - P)} \end{bmatrix}, \tag{78}$$

where C_Υ is a normalization constant and

$$\zeta_\Upsilon = \frac{\zeta_* + iD(n^2\sin^2\alpha - S)(\cos^2\phi - \sin^2\phi)}{|\bar{\lambda}|^2}, \quad (79a)$$

with

$$\zeta_* = \gamma + D^2\cos^2\phi - n^2\cos\alpha\sin\alpha(n^2\sin^2\alpha - S), \quad (79b)$$

$$\gamma = [(n^2\sin^2\alpha - S)^2 + (n^2\cos\alpha\sin\alpha)^2]\sin\phi\cos\phi, \quad (79c)$$

$$\bar{\lambda} = (n^2\sin^2\alpha - S)\cos\phi - (n^2\cos\alpha\sin\alpha + iD)\sin\phi. \quad (79d)$$

The refractive indices in (76) have real and positive roots $\omega_{\perp 1,2}$ associated with $(n_\Upsilon)_+$ and $\omega_{\perp +}$ associated with $(n_\Upsilon)_-$. These frequencies are not presented here as they are very extensive and intricate solutions of a sixth-order equation in frequency.

In the following, some aspects of the indices $(n_\Upsilon)_\pm$ will be discussed. Figures 17 and 18 illustrate the general behavior of $(n_\Upsilon)_\pm$ for $\alpha - \phi = 0$ ($\mathbf{V}\|\mathbf{n}$) and $\alpha - \phi = \pi/2$ ($\mathbf{V}\perp\mathbf{n}$), shown by the red and blue lines, respectively.

1. About the index $(n_\Upsilon)_+$

The refractive index $(n_\Upsilon)_+$ can be compared to the index n_T, given in Eq. (66), which describes the usual transversal mode. We find that $(n_\Upsilon)_+$ has two cutoff frequencies, $\omega_\perp$ and $\omega_{\perp 2}$. The behavior of $(n_\Upsilon)_+$ is illustrated in Fig. 17, which shows the following features:

(i) For $0 < \omega < \omega_\perp$, $(n_\Upsilon)_+$ is imaginary, corresponding to an absorption zone.

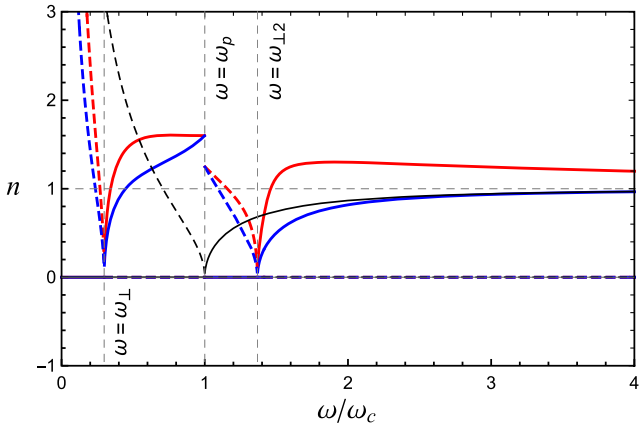

FIG. 17. Red (blue) line indicates the index $(n_\Upsilon)_+$ for $\alpha - \phi = 0$ ($\alpha - \phi = \pi/2$). The black line illustrates n_T. Dashed (solid) lines represent the imaginary (real) pieces of $(n_\Upsilon)_+$ and n_T. The chiral factor allows a new intermediary propagating zone for $\omega_\perp < \omega < \omega_p$, which is followed by a new absorption zone for $\omega_p < \omega < \omega_{\perp 2}$. Here we use $\omega_c = \omega_p$, $|\mathbf{V}| = 2\omega_p$, and $\omega_c = 1$ rad s^{-1}. The black line is the thinnest one (solid and dashed parts). The blue line is lower than the red curve (solid and dashed pieces).

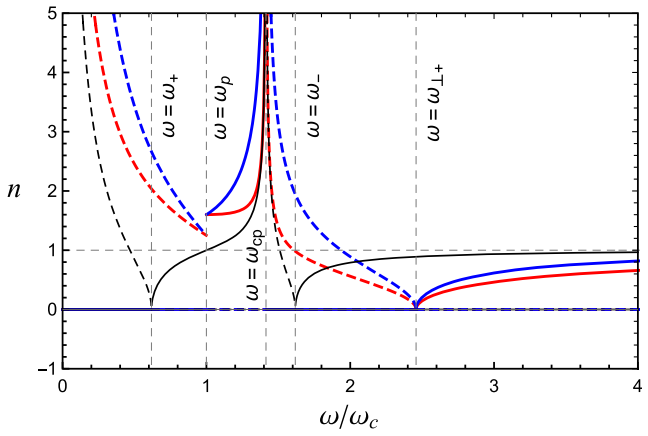

FIG. 18. Red (blue) line: plot of the index $(n_\Upsilon)_-$ for $\alpha - \phi = 0$ ($\alpha - \phi = \pi/2$). Black line: plot of the index n_O. Dashed (solid) lines represent the imaginary (real) pieces of $(n_\Upsilon)_-$ and n_O. The chiral factor enhances the length of the two absorption zones. Here we use $\omega_c = \omega_p$, $|\mathbf{V}| = 2\omega_p$, and $\omega_c = 1$ rad s^{-1}. The black line is the thinnest one (solid and dashed parts). The red line is lower than the blue curve (solid and dashed pieces).

(ii) For $\omega_\perp < \omega < \omega_p$, there is an attenuation-free propagation zone where $\mathrm{Re}[(n_\Upsilon)_+] \neq 0$ and $\mathrm{Im}[(n_\Upsilon)_+] = 0$. In the standard case, there is an absorption zone in this range.

(iii) For $\omega \to \omega_p$, $(n_\Upsilon)_+$ has an unusual discontinuity, as shown in Fig. 17. For $\omega_p < \omega < \omega_{\perp 2}$, the index $(n_\Upsilon)_+$ is imaginary and there is an absorption zone. This aspect contrasts with the usual case, where n_T is always real for $\omega > \omega_p$.

(iv) For $\omega > \omega_{\perp 2}$, $(n_\Upsilon)_+$ is real, yielding an attenuation-free propagation zone.

2. About the index $(n_\Upsilon)_-$

The index $(n_\Upsilon)_-$ is a modification of the index n_O, given in Eq. (8), associated with the usual extraordinary mode. The former has a cutoff frequency at $\omega_{\perp +}$, as shown in Fig. 18. Some aspects of $(n_\Upsilon)_-$ are summarized below.

(i) For $0 < \omega < \omega_p$, there is an absorption zone where $\mathrm{Re}[(n_\Upsilon)_-] = 0$ and $\mathrm{Im}[(n_\Upsilon)_-] \neq 0$. For $\omega \to \omega_p$, $(n_\Upsilon)_-$ has a discontinuity, as noticed in Fig. 18. For $\omega_p < \omega < \omega_{cp}$, the index $(n_\Upsilon)_-$ is real, corresponding to a propagation window. As $\omega_p > \omega_+$, the first absorption zone is enlarged while the first propagating window is shortened.

(ii) For $\omega \to \omega_{cp}$, $(n_\Upsilon)_- \to \infty$, which is the same behavior as in the usual case, as indicated in Fig. 18. For $\omega_{cp} < \omega < \omega_{\perp +}$, the index $(n_\Upsilon)_-$ is purely imaginary and the associated mode is absorbed. As $\omega_{\perp +} > \omega_-$, this second absorption zone is also enlarged in comparison with the usual-case one.

(iii) For $\omega > \omega_{\perp +}$, the quantity $(n_\Upsilon)_-$ is always real, corresponding to an attenuation-free propagation

zone. In the standard case, the propagation zone occurs for $\omega > \omega_-$.

3. Optical effects

For this configuration, there are two elliptical propagating modes associated with the refractive indices $(n_\Upsilon)_\pm$, given in Eq. (76). Thus, the birefringence is measured in terms of the phase shift per unit length,

$$\frac{\Delta}{d} = \frac{2\pi}{\lambda_0}((n_\Upsilon)_+ - (n_\Upsilon)_-). \tag{80}$$

Using the indices (76), the latter becomes

$$\frac{\Delta}{d} = \frac{2\pi}{\lambda_0}(\sqrt{\Pi - \Xi_{\perp-}} - \sqrt{\Pi - \Xi_{\perp+}}), \tag{81}$$

where

$$\Pi = \frac{S(P+S) - D^2}{2S}, \tag{82a}$$

$$\Xi_{\perp\pm}(\omega, |\mathbf{V}|) = \frac{|\mathbf{V}|^2 \sin^2(\alpha - \phi)}{2S\omega^2} \pm \eta/4. \tag{82b}$$

In the high-frequency limit, where $\omega \gg (\omega_c, \omega_p)$, Eq. (81) becomes

$$\frac{\Delta}{d} = \frac{\pi}{\lambda_0}(\sqrt{4 + |\mathbf{V}|\xi_+/\omega^2} - \sqrt{4 + |\mathbf{V}|\xi_-/\omega^2}), \tag{83a}$$

with

$$\xi_\pm = \pm\sqrt{|\mathbf{V}|^2 + 8\omega^2 + \tilde{\gamma}\cos(2(\alpha - \phi))} - 2|\mathbf{V}|^2 \sin^2(\alpha - \phi), \tag{83b}$$

$$\tilde{\gamma} = (8\omega^2 - 2|\mathbf{V}|^2) + |\mathbf{V}|^2 \cos(2(\alpha - \phi)). \tag{83c}$$

In this limit, the usual-case result, $\Delta/d = 0$, is recovered for $|\mathbf{V}| \to 0$.

Considering the lossy effect, one observes that electromagnetic modes associated with the refractive indices $(n_\Upsilon)_\pm$ are absorbed for $\omega < \omega_\perp$ (see the dashed line in Figs. 17 and 18). In this range, we can write the difference of absorption between the two modes per unit length,

$$\frac{\Delta_{\mathrm{Im}}}{d} = \frac{2\pi}{\lambda_0}(\mathrm{Im}[(n_\Upsilon)_+] - \mathrm{Im}[(n_\Upsilon)_-]), \tag{84}$$

or

$$\frac{\Delta_{\mathrm{Im}}}{d} = \frac{2\pi}{\lambda_0}\left(\sqrt{\Xi_{\perp-} - \Pi} - \sqrt{\Xi_{\perp+} - \Pi}\right). \tag{85}$$

For $\omega_{cp} < \omega < \omega_{\perp+}$, only $(n_\Upsilon)_-$ has a non-null imaginary piece. Then, the corresponding absorption coefficient $\gamma = 2\omega\mathrm{Im}[(n_\Upsilon)_-]$ in this range is

$$\gamma = 2\omega\sqrt{\Xi_{\perp+} - \Pi}. \tag{86}$$

On the other hand, for $\omega_p < \omega < \omega_{\perp 2}$, only $(n_\Upsilon)_+$ has an imaginary piece, which implies the following absorption coefficient:

$$\gamma = 2\omega\sqrt{\Xi_{\perp-} - \Pi}. \tag{87}$$

In the usual case, the two electromagnetic modes are absorbed for $\omega < \omega_+$, since the indices n_T and n_O are purely imaginary in this range.

IV. FINAL REMARKS AND PERSPECTIVES

Electromagnetic-wave propagation and absorption in a cold magnetized plasma were analyzed in the case of the spacelike MCFJ theory, which entails the AHE current term, $\mathbf{J}_{AH} = \mathbf{k}_{AF} \times \mathbf{E}$. Here, the background vector represents the chiral factor of the system. Using the usual cold plasma permittivity tensor and the modified Maxwell equations, we obtained the dispersion relation and corresponding refractive indices for two main situations: (i) wave propagation along the magnetic axis (see Sec. II) and (ii) wave propagation orthogonal to the magnetic axis (see Sec. III). These two scenarios were examined for two possible configurations of the chiral vector: longitudinal and orthogonal to the magnetic field.

In Sec. II A, we discussed wave propagation along the magnetic field with the chiral vector in the same direction. The modified refractive indices n_R and n_L were obtained, being associated with RCP and LCP modes, respectively. Their properties were carefully examined in order to determine how the conventional propagation and absorption zones are affected. Figures 1, 2, 3, and 4 display the dispersive behavior of these indices, which are also scrutinized in the plots of the dispersion relations (see Figs. 5, 6, and 7). The appearance of new absorption or propagation zones, as well as the length increase or reduction of these zones, are the main effects induced by the chiral vector. In contrast with the cold plasma under a scalar chiral factor [74], the present plasma model does not manifest negative refraction.

In the very-low-frequency regime, the propagating modes were analyzed and there occurs the possibility of propagating RCP [Eq. (38a)] or LCP helicons [Eq. (38b)], another effect stemming from the chiral vector. However, only one of them can propagate for each choice of the chiral vector magnitude. This is an additional point of distinction in comparison with the cold plasma with a scalar chiral factor of Ref. [74], where both RCP and LCP helicons could propagate simultaneously.

The circular birefringence in Sec. II A was evaluated in terms of the RP for the refractive indices n_R and n_L, under the two conditions for the magnitude of the chiral vector, $|\mathbf{V}| > \omega_p^2/\omega_c$ and $|\mathbf{V}| < \omega_p^2/\omega_c$. The corresponding RPs

are depicted in Figs. 9 and 10, respectively, being the former endowed with sign reversion. Such an inversion occurs in scenarios of rotating plasmas [94], where the RP changes sign and decays as $1/\omega^2$ for high frequencies. It also occurs in the MCFJ chiral plasma with a timelike component, V_0 [74], where the RP reverses and tends to an asymptotic value, $-V_0$. In the present case, an analogous behavior occurs: the RP reverses and tends to the asymptotic value $-|V|/2$. Therefore, it is worth discussing the possibility of using the RP to characterize chiral plasmas described by the effective MCFJ electrodynamics (concerning the scalar or vector chiral factor). In this sense, one can compare the RP of Fig. 9 with that of Fig. 14 of Ref. [74] and note a substantial similarity: both are endowed with sign reversal and asymptotic negative values. The main difference between them takes place near the origin when the former RP tends to zero. Concerning the RP depicted in Fig. 10, the behavior is similar to those of Figs. 15 and 16 of Ref. [74] in the range $0 < \omega < \omega_c$, but different for $\omega > \omega_c$, where the latter become positive due to the negative refraction, while the present RP is negative (see Fig. 10). Thus, we reinforce that the RP behavior may constitute a route to distinguish between the MCFJ cold plasmas with scalar or vector chiral factors, that is, cold plasmas with a magnetic current (CME) and the AHE. As for the absorption zones, the coefficient of circular dichroism reveals a behavior analogous to that of the conventional cold plasma under the condition (35).

In Sec. II B, we considered the case of propagation along the magnetic field and the chiral vector orthogonal to it. The refractive indices were obtained and their properties were examined. The associated modes have mixed transversal and longitudinal components, with elliptical polarization in the transversal sector. Thus, the birefringence and the dichroism were measured in terms of phase shift coefficients per unit length.

The general dispersive behavior of the refractive indices obtained in this case is represented by Figs. 13 and 14. The zones of attenuation-free propagation and absorption are defined by several characteristic frequencies, determined by Eqs. (52) and (53). In comparison with the usual cold plasma scenario, some differences are noted. The dispersive refractive index of Fig. 13 presents two absorption zones with a propagation regime between them. For the case depicted in Fig. 14, the absorption zone is increased by $\Delta\omega = \omega_B - \omega_-$ in relation to the usual case.

The scenario of propagation orthogonal to the magnetic field was addressed in Sec. III, also considering the cases with a chiral vector parallel and orthogonal to the magnetic field. Besides the usual transversal mode of Eq. (66), in Sec. III A we obtained a second refractive index associated with a general elliptically polarized propagating mode. Its dispersive behavior under the condition (35) is represented in Fig. 15, revealing that the chiral vector narrows the first absorption zone and slightly increases the second one, in comparison with the usual cold plasma. For condition (33), the chiral vector shortens the first window of absorption and greatly enhances the second one; see Fig. 16. The birefringence and absorption effects were evaluated in terms of the phase shift of Eq. (72) and the coefficient of Eq. (75), respectively.

In Sec. III B, the case of the chiral vector orthogonal to the magnetic field was discussed. The intricate dispersive behaviors of the refractive indices obtained in this case are represented in Figs. 17 and 18. Compared to the standard cold plasma, we note that in Fig. 17 a new absorption zone appears between the two propagation windows, while the chiral vector decreases the first one. In Fig. 18, the two absorption zones are enlarged compared to the corresponding zones of the usual cold plasma.

General properties of three distinct cold plasma electrodynamics, namely, (i) standard cold plasma, (ii) cold plasma with magnetic current, (iii) cold plasma with anomalous Hall current (the present article), are sumarized in Tables I and II for Faraday and Voigt configurations, respectively, comparing aspects of the propagating modes,

TABLE I. Propagation properties of cold plasmas in distinct contexts for the Faraday configuration ($\mathbf{k}\|\mathbf{B}$). The symbol "$\cdots$" means that the entry does not apply to the mentioned plasma model.

	Cold plasma in usual electrodynamics	Cold plasmas in MCFJ theory with $\mathbf{J}_B = k_{AF}^0\mathbf{B}$	Cold plasmas in MCFJ theory with anomalous Hall current (AHE)	
Propagating modes	RCP and LCP	RCP for $n_{R,M}$, LCP for $n_{L,E}$; see Ref. [74]	$\mathbf{V}\|\mathbf{B}$ LCP and RCP	$\mathbf{V}\perp\mathbf{B}$ Elliptical
Birefringence	RP, $\delta = -\frac{\omega}{2}(\mathrm{Re}[n_+] - \mathrm{Re}[n_-])$	RP δ_{LR} and δ_{ER}; see Ref. [74]	RP (40)	Phase shift (56)
RP inversion	No	Yes	Yes, under the condition (35)	$\cdots$
Absorption	Yes (dichroism)	Yes (dichroism)	Yes, (dichroism) coefficient (46)	Coefficients (60) and (61)
Helicons	RCP	RCP and LCP, enabled by the magnetic current	RCP or LCP (nonsimultaneous); see Eq. (38)	$\cdots$

TABLE II. Propagation properties of cold plasmas in distinct contexts for the Voigt configuration ($\mathbf{k}\perp\mathbf{B}$). The symbol "· · ·" means that the entry does not apply to the mentioned plasma model.

	Cold plasmas in usual electrodynamics	Cold plasmas in MCFJ theory with $\mathbf{J}_B = k_{AF}^0\mathbf{B}$	Cold plasmas in MCFJ theory with anomalous Hall current (AHE)	
Propagating modes	Linear for n_T and elliptical for n_O	Mixed elliptical, in general	$\mathbf{V}\parallel\mathbf{B}$ Elliptical	$\mathbf{V}\perp\mathbf{B}$ Elliptical
Birefringence	Phase shift	Phase shift	Phase shift (72)	Phase shift (81)
RP inversion	· · ·	· · ·	· · ·	· · ·
Absorption	Yes	Yes	Yes, given by Eq. (75)	Yes, given by Eqs. (85), (86), and (87)
Helicons	· · ·	· · ·	· · ·	· · ·

birefringence, RP inversion, absorption, and helicon modes.

It is important to state that the present investigation has led to plasma solutions in a static axion scenario, $\partial_t\theta = 0$, with a spatially dependent axion field,

$$\theta(\mathbf{r}) = \mathbf{V}\cdot\mathbf{r}, \tag{88}$$

such that $\boldsymbol{\nabla}\theta = \mathbf{V} = cte$, similar to the one considered to examine the axionic Casimir-like effect in Ref. [73]. An interesting future perspective consists in examining plasma modes in the context of the axion Lagrangian,

$$\mathcal{L} = -\frac{1}{4}G^{\mu\nu}F_{\mu\nu} + g\theta(\mathbf{E}\cdot\mathbf{B}), \tag{89}$$

and the corresponding equations of motion,

$$\nabla\cdot\mathbf{D} = J^0 - g\boldsymbol{\nabla}\theta\cdot\mathbf{B}, \tag{90}$$

$$\nabla\times\mathbf{H} - \frac{\partial\mathbf{D}}{\partial t} = \mathbf{J} - g(\partial_t\theta)\mathbf{B} + g\boldsymbol{\nabla}\theta\times\mathbf{E}, \tag{91}$$

in a time-dependent scenario. For an oscillating axion field $\theta(t) = \theta_0\exp(i\omega_a t)$, considering a situation in which the axion field oscillates at the same frequency as the electromagnetic field, cold plasma modes may be found by employing the same framework as in the present work. A model with an oscillating axion background was recently considered for examining Casimir forces [99], with an axion field $\theta = \theta_0\sin(\omega_a t)$. A plasma investigation in this time-dependent scenario seems to be a promising perspective. Another possibility is to examine optical properties with astrophysical interest, such as the time of arrival of radio waves from pulsars, in the chiral plasma scenario of the present work and that of Ref. [74]. It may involve the evaluation of group velocity and time delay [100], which can be accomplished in the regime of free propagation for each of the cases examined.

ACKNOWLEDGMENTS

The authors express their gratitude to FAPEMA, CNPq, and CAPES (Brazilian research agencies) for their invaluable financial support. M. M. F. is supported by CNPq/Produtividade 311220/2019-3 and CNPq/Universal/422527/2021-1. P. D. S. S. is grateful to Grant CNPq/PDJ 150584/23. Furthermore, we are indebted to CAPES/Finance Code 001 and FAPEMA/POS-GRAD-02575/21.

[1] A. Zangwill, *Modern Electrodynamics* (Cambridge University Press, New York, 2012).
[2] J. D. Jackson, *Classical Electrodynamics*, 3rd ed. (John Wiley & Sons, New York, 1999).
[3] P. Chabert and N. Braithwaite, *Physics of Radio-Frequency Plasmas* (Cambridge University Press, Cambridge, England, 2011).
[4] E. V. Appleton and G. Builder, The ionosphere as a doubly refracting medium, Proc. Phys. Soc. **45**, 208 (1932); E. V. Appleton, Wireless studies of the ionosphere, J. Inst. Electr. Eng. **7**, 257 (1932).
[5] D. R. Hartree, The propagation of electromagnetic waves in a stratified medium, Math. Proc. Cambridge Philos. Soc. **25**, 97 (1929).

[6] J. A. Ratcliff, The formation of the ionosphere. Ideas of the early years (1925–1955), J. Atmos. Terr. Phys. **36**, 2167 (1974).
[7] L. J. Guo, L. X. Guo, and J. T. Li, Propagation of terahertz electromagnetic waves in a magnetized plasma with inhomogeneous electron density and collision frequency, Phys. Plasmas **24**, 022108 (2017).
[8] D. A. Gurnett and A. Bhattacharjee, *Introduction to Plasma Physics* (Cambridge University Press, Cambridge, England, 2005).
[9] P. A. Sturrock, *Plasma Physics: An Introduction to the Theory of Astrophysical, Geophysical and Laboratory Plasmas* (Cambridge University Press, Cambridge, England, 1994).
[10] J. A. Bittencourt, *Fundamentals of Plasma Physics*, 3rd ed. (Springer, New York, 2004).
[11] T. H. Stix, *Waves in Plasmas* (Springer, New York, 1992).
[12] A. Piel, *Plasmas Physics—An Introduction to Laboratory, Space, and Fusion Plasmas* (Springer, Heidelberg, 2010).
[13] T. J. M. Boyd and J. J. Sanderson, *The Physics of Plasmas* (Cambridge University Press, New York, 2003).
[14] Y. Tang and A. E. Cohen, Optical chirality and its interaction with matter, Phys. Rev. Lett. **104**, 163901 (2010).
[15] A. H. Sihvola and I. V. Lindell, Bi-isotropic constitutive relations, Microwave Opt. Technol. Lett., **4**, 295 (1991); A. H. Sihvola and I. V. Lindell, Properties of bi-isotropic Fresnel reflection coefficients, Opt. Commun. **89**, 1 (1992); S. Ougier, I. Chenerie, A. Sihvola, and A. Priou, Propagation in bi-isotropic media: Effect of different formalisms on the propagation analysis, Prog. Electromagn. Res. **09**, 19 (1994).
[16] P. Hillion, Manifestly covariant formalism for electromagnetism in chiral media, Phys. Rev. E **47**, 1365 (1993); Y. Itin, Dispersion relation for electromagnetic waves in anisotropic media, Phys. Lett. A **374**, 1113 (2010); N. J. Damaskos, A. L. Maffett, and P. L. E. Uslenghi, Dispersion relation for general anisotropic media, IEEE Trans. Antennas Propagat. **AP-30**, 991 (1982).
[17] J. A. Kong, *Electromagnetic Wave Theory* (Wiley, New York, 1986).
[18] Y. T. Aladadi and M. A. S. Alkanhal, Classification and characterization of electromagnetic materials, Sci. Rep. **10**, 11406 (2020).
[19] W. Mahmood and Q. Zhao, The double Jones birefringence in magneto-electric medium, Sci. Rep. **5**, 13963 (2015).
[20] V. A. De Lorenci and G. P. Goulart, Magnetoelectric birefringence revisited, Phys. Rev. D **78**, 045015 (2008).
[21] P. D. S. Silva, R. Casana, and M. M. Ferreira Jr., Symmetric and antisymmetric constitutive tensors for bi-isotropic and bi-anisotropic media, Phys. Rev. A **106**, 042205 (2022).
[22] G. R. Fowles, *Introduction to modern optics*, 2nd ed. (Dover Publications, INC., New York, 1975); A. K. Bain, *Crystal Optics: Properties and Applications* (Wiley-VCH Verlag GmbH & Co. KGaA, Germany, 2019).
[23] H. S. Bennett and E. A. Stern, Faraday effect in solids, Phys. Rev. **137**, A448 (1965); L. M. Roth, Theory of the Faraday effect in solids, Phys. Rev. **133**, A542 (1964).
[24] W. S. Porter and E. M. Bock Jr., Faraday effect in a plasma, Am. J. Phys. **33**, 1070 (1965).
[25] J. Shibata, A. Takeuchi, H. Kohno, and G. Tatara, Theory of electromagnetic wave propagation in ferromagnetic Rashba conductor, J. App. Phys. **123**, 063902 (2018).
[26] E. U. Condon, Theories of optical rotatory power, Rev. Mod. Phys. **9**, 432 (1937).
[27] Ming-Che Chang and Min-Fong Yang, Optical signature of topological insulators, Phys. Rev. B **80**, 113304 (2009); L. Ohnoutek *et al.*, Strong interband Faraday rotation in 3D topological insulator Bi_2Se_3, Sci. Rep. **6**, 19087 (2016).
[28] A. Martín-Ruiz, M. Cambiaso, and L. F. Urrutia, The magnetoelectric coupling in electrodynamics, Int. J. Mod. Phys. A **34**, 1941002 (2019); A. Martín-Ruiz, M. Cambiaso, and L. F. Urrutia, Electro- and magnetostatics of topological insulators as modeled by planar, spherical, and cylindrical θ boundaries: Green's function approach, Phys. Rev. D **93**, 045022 (2016).
[29] A. Martín-Ruiz, M. Cambiaso, and L. F. Urrutia, A Green's function approach to the Casimir effect on topological insulators with planar symmetry, Eur. Phys. Lett. **113**, 60005 (2016); A. Martín-Ruiz, M. Cambiaso, and L. F. Urrutia, Green's function approach to Chern-Simons extended electrodynamics: An effective theory describing topological insulators, Phys. Rev. D **92**, 125015 (2015).
[30] A. Martín-Ruiz, M. Cambiaso, and L. F. Urrutia, Electromagnetic description of three-dimensional time-reversal invariant ponderable topological insulators, Phys. Rev. D **94**, 085019 (2016); A. Martín-Ruiz, Magnetoelectric effect in cylindrical topological insulators, Phys. Rev. D **98**, 056012 (2018).
[31] A. Lakhtakia and T. G. Mackay, Classical electromagnetic model of surface states in topological insulators, J. Nanophoton. **10**, 033004 (2016).
[32] T. M. Melo, D. R. Viana, W. A. Moura-Melo, J. M. Fonseca, and A. R. Pereira, Topological cutoff frequency in a slab waveguide: Penetration length in topological insulator walls, Phys. Lett. A **380**, 973 (2016).
[33] Z.-X. Li, Yunshan Cao, and Peng Yan, Topological insulators and semimetals in classical magnetic systems, Phys. Rep. **915**, 1 (2021).
[34] R. Li, J. Wang, Xiao-Liang Qi, and S.-C. Zhang, Dynamical axion field in topological magnetic insulators, Nat. Phys. **6**, 284 (2010).
[35] W.-K. Tse and A. H. MacDonald, Giant magneto-optical Kerr effect and universal Faraday effect in thin-film topological insulators, Phys. Rev. Lett. **105**, 057401 (2010); Magneto-optical and magnetoelectric effects of topological insulators in quantizing magnetic fields, Phys. Rev. B **82**, 161104 (2010); Magneto-optical Faraday and Kerr effects in topological insulator films and in other layered quantized Hall systems, Phys. Rev. B **84**, 205327 (2011).
[36] I. Crassee, J. Levallois, A. L. Walter, M. Ostler, A. Bostwick, E. Rotenberg, T. Seyller, D. van der Marel, and A. B. Kuzmenko, Giant Faraday rotation in single- and multilayer graphene, Nat. Phys. **7**, 48 (2011); R. Shimano, G. Yumoto, J. Y. Yoo, R. Matsunaga, S. Tanabe, H. Hibino, T. Morimoto, and H. Aoki, Quantum Faraday and Kerr rotations in graphene, Nat. Commun. **4**, 1841 (2013).

[37] S. M. Carroll, G. B. Field, and R. Jackiw, Limits on a Lorentz- and parity-violating modification of electrodynamics, Phys. Rev. D **41**, 1231 (1990).

[38] D. Colladay and V. A. Kostelecký, *CPT* violation and the Standard Model, Phys. Rev. D **55**, 6760 (1997); D. Colladay and V. A. Kostelecký, Lorentz-violating extension of the Standard Model, Phys. Rev. D **58**, 116002 (1998); S. R. Coleman and S. L. Glashow, High-energy tests of Lorentz invariance, Phys. Rev. D **59**, 116008 (1999).

[39] J. Alfaro, A. A. Andrianov, M. Cambiaso, P. Giacconi, and R. Soldati, Bare and induced Lorentz and *CPT* invariance violations in QED, Int. J. Mod. Phys. A **25**, 3271 (2010); A. A. Andrianov, D. Espriu, P. Giacconi, and R. Soldati, Anomalous positron excess from Lorentz-violating QED, J. High Energy Phys. 09 (2009) 057.

[40] L. C. T. Brito, J. C. C. Felipe, A. Yu. Petrov, and A. P. Baeta Scarpelli, No radiative corrections to the Carroll-Field-Jackiw term beyond one-loop order, Int. J. Mod. Phys. A **36**, 2150033 (2021); J. F. Assuncao, T. Mariz, and A. Yu. Petrov, Non-analyticity of the induced Carroll-Field-Jackiw term at finite temperature, Europhys. Lett. **116**, 31003 (2016); J. C. C. Felipe, A. R. Vieira, A. L. Cherchiglia, A. P. Baêta Scarpelli, and M. Sampaio, Arbitrariness in the gravitational Chern-Simons-like term induced radiatively, Phys. Rev. D **89**, 105034 (2014); T. R. S. Santos and R. F. Sobreiro, Lorentz-violating Yang–Mills theory: Discussing the Chern–Simons-like term generation, Eur. Phys. J. C **77**, 903 (2017).

[41] R. Casana, M. M. Ferreira Jr., E. da Hora, and A. B. F. Neves, Maxwell-Chern-Simons vortices in a CPT-odd Lorentz-violating Higgs electrodynamics, Eur. Phys. J. C **74**, 3064 (2014); R. Casana and L. Sourrouille, Self-dual Maxwell-Chern-Simons solitons from a Lorentz-violating model, Phys. Lett. B **726**, 488 (2013).

[42] H. Belich, L. D. Bernald, Patricio Gaete, and J. A. Helayël-Neto, The photino sector and a confining potential in a supersymetric Lorentz-symmetry-violating model, Eur. Phys. J. C **73**, 2632 (2013); L. Bonetti, L. R. dos Santos Filho, J A. Helayël-Neto, and A. D. A. M. Spallicci, Photon sector analysis of Super and Lorentz symmetry breaking: Effective photon mass, bi-refringence and dissipation, Eur. Phys. J. C **78**, 811 (2018).

[43] R. Lehnert and R. Potting, Vacuum Cherenkov radiation, Phys. Rev. Lett. **93**, 110402 (2004); R. Lehnert and R. Potting, Cherenkov effcet in Lorentz-violating vacua, Phys. Rev. D **70**, 125010 (2004); **70**, 129906(E) (2004).

[44] B. Altschul, Chrenkov radiation in a Lorentz-violating and birefringent vacuum, Phys. Rev. D **75**, 105003 (2007).

[45] O. J. Franca, L. F. Urrutia, and O. Rodríguez-Tzompantzi, Reversed electromagnetic Cherenkov radiation in naturally existing magnetoelectric media, Phys. Rev. D **99**, 116020 (2019); E. Barredo-Alamilla, L. F. Urrutia, and M. M. Ferreira Jr., Electromagnetic radiation in chiral matter: The Cherenkov case, Phys. Rev. D **107**, 096024 (2023).

[46] L. H. C. Borges and A. F. Ferrari, External sources in a minimal and nonminimal CPT-odd Lorentz violating Maxwell electrodynamics, Mod. Phys. Lett. A **37**, 2250021 (2022); Y. M. P. Gomes and P. C. Malta, Lab-based limits on the Carroll-Field-Jackiw Lorentz-violating electrodynamics, Phys. Rev. D **94**, 025031 (2016); M. M. Ferreira Jr, J. A. Helayël-Neto, C. M. Reyes, M. Schreck, and P. D. S. Silva, Unitarity in Stückelberg electrodynamics modified by a Carroll-Field-Jackiw term, Phys. Lett. B **804**, 135379 (2020); A. Martín-Ruiz and C. A. Escobar, Local effects of the quantum vacuum in Lorentz-violating electrodynamics, Phys. Rev. D **95**, 036011 (2017); P. Sikivie, Invisible axion search methods, Rev. Mod. Phys. **93**, 015004 (2021).

[47] A. Sekine and K. Nomura, Axion electrodynamics in topological materials, J. Appl. Phys. **129**, 141101 (2021).

[48] M. E. Tobar, B. T. McAllister, and M. Goryachev, Modified axion electrodynamics as impressed electromagnetic sources through oscillating background polarization and magnetization, Phys. Dark Universe **26**, 100339 (2019).

[49] E. J. Post, *Formal Structure of Electromagnetics: General Covariance and Electromagnetics* (Norht-Holland Publishing Company, Amsterdam, Dover Publication, 1997).

[50] Z. Qiu, G. Cao, and X.-G. Huang, Electrodynamics of chiral matter, Phys. Rev. D **95**, 036002 (2017).

[51] D. E. Kharzeev, The chiral magnetic effect and anomaly-induced transport, Prog. Part. Nucl. Phys. **75**, 133 (2014); D. E. Kharzeev, J. Liao, S. A. Voloshin, and G. Wang, Chiral magnetic and vortical effects in high-energy nuclear collisions—A status report, Prog. Part. Nucl. Phys. **88**, 1 (2016).

[52] K. Fukushima, D. E. Kharzeev, and H. J. Warringa, Chiral magnetic effect, Phys. Rev. D **78**, 074033 (2008); D. E. Kharzeev and H. J. Warringa, Chiral magnetic conductivity, Phys. Rev. D **80**, 034028 (2009).

[53] A. Vilenkin, Equilibrium parity-violating current in a magnetic field, Phys. Rev. D **22**, 3080 (1980); A. Vilenkin and D. A. Leahy, Parity nonconservation and the origin of cosmic magnetic fields, Astrophys. J. **254**, 77 (1982).

[54] J. Schober, A. Brandenburg, and I. Rogachevskii, Chiral fermion asymmetry in high-energy plasma simulations, Geophys. Astrophys. Fluid Dyn. **114**, 106 (2020).

[55] M. Dvornikov and V. B. Semikoz, Influence of the turbulent motion on the chiral magnetic effect in the early universe, Phys. Rev. D **95**, 043538 (2017).

[56] G. Sigl and N. Leite, Chiral magnetic effect in protoneutron stars and magnetic field spectral evolution, J. Cosmol. Astropart. Phys. 01 (2016) 025.

[57] M. Dvornikov and V. B. Semikoz, Magnetic field instability in a neutron star driven by the electroweak electron-nucleon interaction versus the chiral magnetic effect, Phys. Rev. D **91**, 061301(R) (2015).

[58] M. Dvornikov and V. B. Semikoz, Instability of magnetic fields in electroweak plasma driven by neutrino asymmetries, J. Cosmol. Astropart. Phys. 05 (2014) 002; M. Dvornikov, Electric current induced by an external magnetic field in the presence of electroweak matter, EPJ Web Conf. **191**, 05008 (2018).

[59] A. A. Burkov, Chiral anomaly and transport in Weyl metals, J. Phys. Condens. Matter **27**, 113201 (2015).

[60] E. Barnes, J. J. Heremans, and Djordje Minic, Electromagnetic signatures of the chiral anomaly in Weyl semimetals, Phys. Rev. Lett. **117**, 217204 (2016).

[61] X. Huang, L. Zhao, Y. Long, P. Wang, D. Chen, Z. Yang, H. Liang, M. Xue, H. Weng, Z. Fang, X. Dai, and G. Chen, Observation of the chiral-anomaly-induced negative magnetoresistance in 3D Weyl semimetal TaAs, Phys. Rev. X **5**, 031023 (2015).
[62] C.-X. Liu, P. Ye, and X.-L. Qi, Chiral gauge field and axial anomaly in a Weyl semimetal, Phys. Rev. B **87**, 235306 (2013).
[63] F. D. M. Haldane, Berry curvature on the Fermi surface: Anomalous Hall effect as a topological Fermi-liquid property, Phys. Rev. Lett. **93**, 206602 (2004).
[64] D. Xiao, M. Chang, and Q. Niu, Berry phase effects on electronic properties, Rev. Mod. Phys. **82**, 1959 (2010).
[65] X. G. Huang, Simulating chiral magnetic and separation effects with spin-orbit coupled atomic gases, Sci. Rep. **6**, 20601 (2016).
[66] S. Nakatsuji, N. Kiyohara, and T. Higo, Large anomalous Hall effect in a non-collinear antiferromagnet at room temperature, Nature (London) **527**, 212 (2015).
[67] H. Chen, Q. Niu, and A. H. MacDonald, Anomalous Hall effect arising from noncollinear antiferromagnetism, Phys. Rev. Lett. **112**, 017205 (2014).
[68] Y. Machida, S. Nakatsuji, S. Onoda, T. Tayama, and T. Sakakibara, Time-reversal symmetry breaking and spontaneous Hall effect without magnetic dipole order, Nature (London) **463**, 210 (2010).
[69] R. Côté, R. N. Duchesne, G. D. Duchesne, and O. Trépanier, Chiral filtration and Faraday rotation in multi-Weyl semimetals, Results Phys. **54**, 107064 (2023).
[70] O. Trépanier, R. N. Duchesne, J. J. Boudreault, and R. Côté, Magneto-optical Kerr effect in Weyl semimetals with broken inversion and time-reversal symmetries, Phys. Rev. B **106**, 125104 (2022).
[71] O. V. Bugaiko, E. V. Gorbar, and P. O. Sukhachov, Surface plasmon polaritons in strained Weyl semimetals, Phys. Rev. B **102**, 085426 (2020).
[72] P. D. S. Silva, L. L. Santos, M. M. Ferreira Jr., and M. Schreck, Effects of CPT-odd terms of dimensions three and five on electromagnetic propagation in continuous matter, Phys. Rev. D **104**, 116023 (2021).
[73] I. Brevik, Axion electrodynamics and the axionic Casimir effect, Universe **7**, 133 (2021).
[74] Filipe S. Ribeiro, Pedro D. S. Silva, and M. M. Ferreira Jr., Cold plasma modes in the chiral Maxwell-Carroll-Field-Jackiw electrodynamics, Phys. Rev. D **107**, 096018 (2023).
[75] A. K. Zvezdin and V. A. Kotov, *Modern Magnetooptics and Magnetooptical Materials* (Institute of Physics Publishing, London, 1997).
[76] B. Guo, Chirality-induced negative refraction in magnetized plasma, Phys. Plasmas **20**, 093596 (2013).
[77] M. X. Gao, B. Guo, L. Peng, and X. Cai, Dispersion relations for electromagnetic wave propagation in chiral plasmas, Phys. Plasmas **21**, 114501 (2014).
[78] D. G. Dimitriu and D. O. Dorohoi, New method to determine the optical rotatory dispersion of inorganic crystals applied to some samples of Carpathian Quartz, Spectrochim. Acta, Part A **131**, 674 (2014).
[79] L. A. Pajdzik and A. M. Glazer, Three-dimensional birefringence imaging with a microscope tilting-stage. I. Uniaxial crystals, J. Appl. Crystallogr. **39**, 326 (2006).
[80] X. Liu, J. Yang, Z. Geng, and H. Jia, Simultaneous measurement of optical rotation dispersion and absorption spectra for chiral substances, Chirality **8**, 1071 (2022).
[81] L. D. Barron, *Molecular Light Scattering and Optical Activity*, 2nd ed. (Cambridge University Press, New York, 2004).
[82] J.-M. Poumirol, P. Q. Liu, T. M. Slipchenko, A. Y. Nikitin, L. Martin-Morento, J. Faist, and A. B. Kuzmenko, Electrically controlled terahertz magneto-optical phenomena in continuous and patterned graphene, Nat. Commun. **8**, 14626 (2017).
[83] I. Tutunnikov, U. Steinitz, E. Gershnabel, J.-M. Hartmann, A. A. Milner, V. Milner, and I. Sh. Averbukh, Rotation of the polarization of light as a tool for investigating the collisional transfer of angular momentum from rotating molecules to macroscopic gas flows, Phys. Rev. Res. **4**, 013212 (2022); U. Steinitz and I. Sh. Averbukh, Giant polarization drag in a gas of molecular super-rotors, Phys. Rev. A **101**, 021404(R) (2020).
[84] J. H. Woo, B. K. M. Gwon, J. H. Lee, D-W. Kim, W. Jo, D. H. Kim, and J. W. Wu, Time-resolved pump-probe measurement of optical rotatory dispersion in chiral metamaterial, Adv. Opt. Mater. **5**, 1700141 (2017).
[85] Q. Zhang, E. Plum, J.-Y. Ou, H. Pi, J. Li, K. F. MacDonald, and N. I. Zheludev, Electrogyration in metamaterials: Chirality and polarization rotatory power that depend on applied electric field, Adv. Opt. Mater. **9**, 2001826 (2021).
[86] J. Mun, M. Kim, Y. Yang, T. Badloe, J. Ni, Y. Chen, C.-W. Qiu, and J. Rho, Electromagnetic chirality: From fundamentals to nontraditional chiroptical phenomena, Light Sci. Appl. **9**, 139 (2020).
[87] J. Ma and D. A. Pesin, Dynamic chiral magnetic effect and Faraday rotation in macroscopically disordered helical metals, Phys. Rev. Lett. **118**, 107401 (2017).
[88] U. Dey, S. Nandy, and A. Taraphder, Dynamic chiral magnetic effect and anisotropic natural optical activity of tilted Weyl semimetals, Sci. Rep. **10**, 2699 (2020).
[89] R. Gueroult, Y. Shi, J-M. Rax, and N. J. Fisch, Determining the rotation direction in pulsars, Nat. Commun. **10**, 3232 (2019).
[90] N. Tischler, M. Krenn, R. Fickler, X. Vidal, A. Zeilinger, and G. Molina-Terriza, Quantum optical rotatory dispersion, Sci. Adv. **2**, e1601306 (2016).
[91] L. Tschugaeff, Anomalous rotatory dispersion, Trans. Faraday Soc. **10**, 70 (1914).
[92] R. E. Newnham, *Properties of Materials—Anisotropy, Symmetry, Structure* (Oxford University Press, New York, 2005).
[93] P. D. S. Silva and M. M. Ferreira Jr., Rotatory power reversal induced by magnetic current in bi-isotropic media, Phys. Rev. B **106**, 144430 (2022).
[94] R. Gueroult, J.-M. Rax, and N. J. Fisch, Enhanced tuneable rotatory power in a rotating plasma, Phys. Rev. E **102**, 051202(R) (2020).
[95] P. Hosur and X.-L. Qi, Tunable circular dichroism due to the chiral anomaly in Weyl semimetals, Phys. Rev. B **91**, 081106(R) (2015).
[96] M. Nieto-Vesperinas, Optical theorem for the conservation of electromagnetic helicity: Significance for molecular

energy transfer and enantiomeric discrimination by circular dichroism, Phys. Rev. A **92**, 023813 (2015).
[97] Y. Tang and A. E. Cohen, Enhanced enantioselectivity in excitation of chiral molecules by superchiral light, Science **332**, 333 (2011).
[98] M. Amin, O. Siddiqui, and M. Farhat, Linear and circular dichroism in graphene-based reflectors for polarization control, Phys. Rev. Appl. **13**, 024046 (2020).
[99] A. M. Favitta, I. H. Brevik, and M. M. Chaichian, Axion electrodynamics: Green's functions, zero-point energy and optical activity, Ann. Phys. (Amsterdam) **455**, 169396 (2023).
[100] J. I. McDonald and L. B. Ventura, Optical properties of dynamical axion backgrounds, Phys. Rev. D **101**, 123503 (2020).